

# Small Non-Negative Stencils for Anisotropic Diffusion \*

Jérôme Fehrenbach<sup>†</sup>

Jean-Marie Mirebeau<sup>‡</sup>

April 30, 2022

## Abstract

We introduce a new discretization scheme for Anisotropic Diffusion, AD-LBR, on two and three dimensional cartesian grids. The main features of this scheme is that it is non-negative, and has a stencil size bounded by 6 in 2D, by 14 in 3D, despite allowing diffusion tensors of arbitrary anisotropy. It also has good spectral properties, which permits larger time steps and avoids e.g. chessboard artifacts.

AD-LBR relies on Lattice Basis Reduction, a tool from discrete mathematics which has recently shown its relevance for the discretization on grids of strongly anisotropic Partial Differential Equations [6, 7]. We prove that AD-LBR is in 2D asymptotically equivalent to a finite element discretization on an anisotropic Delaunay triangulation, a procedure more involved and computationally expensive. Our scheme thus benefits from the theoretical guarantees of this procedure, for a fraction of its cost. Numerical experiments in 2D and 3D illustrate our results.

**Keywords:** Anisotropic Diffusion · Non-Negative Numerical Scheme · Lattice Basis Reduction.

We consider throughout this paper a bounded smooth domain  $\Omega \subset \mathbb{R}^d$ , where  $d \in \{2, 3\}$  denotes the dimension, equipped with a continuous diffusion tensor  $\mathbf{D}$ . We do not impose any bound on the diffusion tensor anisotropy, and we are in fact interested in pronounced, non axis-aligned anisotropies. Anisotropic diffusion is here understood in the sense of [14]: the diffusion tensor  $\mathbf{D}(z)$ , at a point  $z \in \Omega$ , is a symmetric positive definite matrix which eigenvalues may have different orders of magnitude. Our results are not relevant for isotropic diffusion with a variable scalar coefficient, as in the pioneering work of Perona and Malik [11].

We address the discretization of the following energy  $\mathcal{E}$ ,

defined for  $u \in H^1(\Omega)$ :

$$\mathcal{E}(u) := \int_{\Omega} \|\nabla u(z)\|_{\mathbf{D}(z)}^2 dz. \quad (1)$$

We denote  $\|e\|_M := \sqrt{\langle e, Me \rangle}$ , for any  $e \in \mathbb{R}^d$ , and any  $M$  in the set  $S_d^+$  of symmetric positive definite  $d \times d$  matrices. Gradient descent for the energy (1) has the form of a parabolic PDE:

$$\partial_t u = \operatorname{div}(\mathbf{D} \nabla u). \quad (2)$$

This equation, Anisotropic Diffusion, is with its variants at the foundation of powerful image processing techniques. Some variants include curvature terms [10], or diffusion-reaction terms [2]. Time varying and solution dependent diffusion tensors can also be considered. A general exposition can be found in [14], where various choices for the definition of the diffusion tensor  $\mathbf{D}$  from the image  $u$ , adapted to various applications, are proposed and discussed.

Our contribution in the discretization of the energy (1) results in improved numerical solutions of (2), in terms accuracy and stability, for a minor increase in complexity. This extends to applications, such as Coherence Enhancing Diffusion, see the numerical experiments in §4, which involve solving (2) using a solution dependent diffusion tensor  $\mathbf{D} = \mathbf{D}_u$ ; regardless of the fact that the resulting nonlinear PDE  $\partial_t u = \operatorname{div}(\mathbf{D}_u \nabla u)$  may not anymore be the gradient descent of an energy. In these applications, the diffusion tensor  $\mathbf{D}_u$  is typically defined in terms of the structure tensor [14] of  $u$ , in such way that diffusion is pronounced within image homogeneous regions, and *tangentially* along image edges, but not across edges.

The 2-dimensional anisotropic diffusion is discussed in [14] (chapter 3), where it is proved that a nonnegative scheme exists for a stencil of size  $(2m + 1) \times (2m + 1)$ , where  $m$  depends on the anisotropy of the diffusion tensor. On the other hand, our approach provides a stencil composed of 6 points with non-negative weights. The distance from these points to the stencil center depends on the anisotropy of the tensor, see Remark 1.

Consider a scale parameter  $h > 0$ , and a sampling  $\Omega_h$  of the domain  $\Omega$  on the cartesian grid  $\mathbb{Z}^d$ , rescaled by  $h$ : with obvious notations

$$\Omega_h := \Omega \cap h\mathbb{Z}^d.$$

\*This work was partly supported by ANR grant MESANGE ANR-08-BLAN-0198.

<sup>†</sup>Institut de Mathématiques de Toulouse Université Paul Sabatier, 31062 TOULOUSE CEDEX 9, France

<sup>‡</sup>CNRS, Laboratory CEREMADE, UMR 7534, University Paris Dauphine, Place du Maréchal De Lattre De Tassigny 75775 PARIS CEDEX 16, France

We introduce a novel discretization of the energy (1), referred to as AD-LBR (Anisotropic Diffusion using Lattice Basis Reduction). It is a sum of squared differences of a discrete map  $u \in L^2(\Omega_h)$

$$\mathcal{E}_h(u) := h^{d-2} \sum_{z \in \Omega_h} \sum_{e \in V(z)} \gamma_z(e) |u(z+he) - u(z)|^2 \quad (3)$$

The stencils  $V(z) \subset \mathbb{Z}^d$ ,  $z \in \Omega_h$ , are symmetric and have cardinality at most 6 in 2D, 14 in 3D. The coefficients  $\gamma_z(e) \geq 0$  are non-negative. They are constructed using a classical tool from discrete mathematics, Lattice Basis Reduction, which allows to cheaply build very efficient stencils for grid discretizations of Partial Differential Equations (PDEs) involving strongly anisotropic diffusion tensors or Riemannian metrics. This approach was applied to anisotropic static Hamilton Jacobi PDEs in [6, 7], resulting in a new numerical scheme: Fast Marching using Lattice Basis Reduction (FM-LBR). Substantial improvements were obtained in comparison with earlier methods, in terms of both accuracy and complexity.

The paper is organized as follows. We describe the stencils of the two dimensional AD-LBR in §1, and state our main 2D result: the asymptotic equivalence of the AD-LBR with a finite element discretization on an Anisotropic Delaunay Triangulation. Section §2 is devoted to the construction of the three dimensional stencils of the AD-LBR, and the proof of the coefficients non-negativity. The more technical §3 details the proof of the 2D equivalence result stated in §1. Two and three dimensional numerical experiments are presented in §4, including qualitative and quantitative comparisons with four other numerical schemes.

## 1 Description of the scheme, and main results

Our numerical scheme, Anisotropic Diffusion using Lattice Basis Reduction (AD-LBR), involves the construction of stencils which geometry is tailored after the local diffusion tensor. This diffusion tensor  $\mathbf{D}$  is meant to measure gradients, as in (1). We shall measure vectors through its inverse  $\mathbf{M}$ , which we regard as a Riemannian<sup>1</sup> metric: for all  $z \in \Omega$

$$\mathbf{M}(z) = \mathbf{D}(z)^{-1}.$$

An essential feature of AD-LBR is its non-negativity: the discrete energy  $\mathcal{E}_h(u)$  is written as a sum (3) of squared differences of values of  $u$ , with non-negative weights  $\gamma_z(e) \geq 0$ . This discretization is consistent if for each  $z \in \Omega_h$ , and any smooth  $u$ ,

$$h^d \|\nabla u(z)\|_{\mathbf{D}(z)}^2 = h^{d-2} \sum_{e \in V(z)} \gamma_z(e) \langle \nabla u(z), he \rangle^2. \quad (4)$$

<sup>1</sup>The Laplace Beltrami operator associated to  $\mathbf{M}$  does *not* coincide with  $\text{div}(\mathbf{D} \nabla \cdot)$ , unless  $\mathbf{D}$  is identically of determinant 1. This is not an issue for our application.

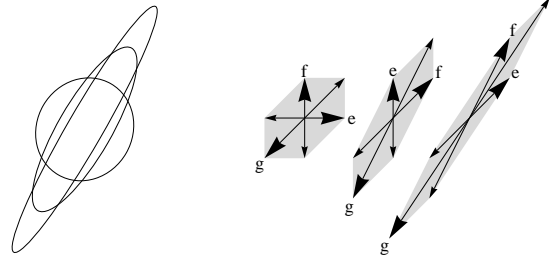


Figure 1: Right : the stencils associated to three matrices  $M$  of anisotropy ratios  $\kappa(M)$  equal to 1.1, 3.5, 8 respectively. The ellipses  $\{z \in \mathbb{R}^2; \|z\|_M = 1\}$  are shown left; their principal axis is aligned with  $(\cos(\pi/3), \sin(\pi/3))$ . More stencils are shown in [6].

Indeed, the left hand side approximates the contribution of the “voxel”  $z + [-h/2, h/2]^d$  to the integral (1), while the right hand side is obtained by injecting the first order approximation  $u(z+he) \simeq u(z) + \langle \nabla u(z), he \rangle$  in (3). The identity (4) is in turn equivalent to

$$\mathbf{D}(z) = \sum_{e \in V(z)} \gamma_z(e) ee^T. \quad (5)$$

The next lemma shows how to obtain such a decomposition in 2D. We denote by  $u^\perp := (-b, a)$  the rotation of a vector  $u = (a, b) \in \mathbb{R}^2$  by  $\pi/2$ , in such way that for all  $v \in \mathbb{R}^2$ :

$$\langle u^\perp, v \rangle = \det(u, v).$$

**Lemma 1.** *Let  $e_1, e_2, e_3 \in \mathbb{R}^2$  be such that  $e_1 + e_2 + e_3 = 0$ , and that  $\alpha := \det(e_1, e_2)$  is non-zero. Then for any  $M \in S_2^+$ :*

$$M^{-1} = 2 \sum_{1 \leq i \leq 3} \gamma_i e_i e_i^T, \quad \text{with } \gamma_i := \frac{-\langle e_{i+1}, M e_{i+2} \rangle}{2\alpha^2 \det(M)}. \quad (6)$$

*Proof.* Note that  $\alpha = \det(e_2, e_3) = \det(e_3, e_1)$ .

We first assume that  $M$  is the identity matrix  $\text{Id}$ . Denoting  $D := 2 \sum_{i=1}^3 \gamma_i e_i e_i^T$ , we obtain

$$\begin{aligned} \langle e_1^\perp, D e_1^\perp \rangle &= 2 \sum_{1 \leq i \leq 3} \gamma_i \langle e_i, e_1^\perp \rangle^2 = 2 \sum_{1 \leq i \leq 3} \gamma_i \det(e_i, e_1)^2 \\ &= 2\alpha^2(\gamma_2 + \gamma_3) = -\langle e_1, e_2 + e_3 \rangle = \|e_1\|^2. \end{aligned}$$

Thus  $\langle e_1^\perp, D e_1^\perp \rangle = \|e_1^\perp\|^2$ . Likewise  $\langle e_2^\perp, D e_2^\perp \rangle = \|e_2^\perp\|^2$ , and  $\langle e_1^\perp + e_2^\perp, D(e_1^\perp + e_2^\perp) \rangle = \langle e_3^\perp, D e_3^\perp \rangle = \|e_3^\perp\|^2 = \|e_1^\perp + e_2^\perp\|^2$ . Since  $(e_1^\perp, e_2^\perp)$  is a basis of  $\mathbb{R}^2$ , it follows that  $D = \text{Id}$ , which establishes (6).

In the case  $M \neq \text{Id}$ , we obtain (6) by applying the above to  $e'_i := M^{\frac{1}{2}} e_i$ , and  $M' := \text{Id}$ .  $\square$

The AD-LBR is based on decompositions (5) similar to the previous lemma, but with *non-negative weights*. This

construction is discussed below in the 2D case, see §2 for the 3D case. For that purpose we introduce a classical tool of discrete geometry: lattice basis reduction, see [9] and references therein. A basis of the lattice  $\mathbb{Z}^2$  is a pair  $(e, f)$  of elements of  $\mathbb{Z}^2$ , which satisfies

$$|\det(e, f)| = 1. \quad (7)$$

If  $(e, f)$  is a basis of  $\mathbb{Z}^2$ , then any  $g \in \mathbb{Z}^2$  can be expressed as a linear combination  $g = \alpha e + \beta f$ , with integer coefficients  $\alpha, \beta \in \mathbb{Z}$ . Note also that the coordinates of  $e$  are co-prime: if  $e = (e_1, e_2)$  then  $\gcd(e_1, e_2) = 1$ , and likewise for  $f$ . Our discretization scheme involves privileged *reduced* bases [9], associated to the local metric.

Consider a fixed symmetric positive definite matrix  $M \in S_2^+$ . The first Minkowski minimum  $\lambda_1(M)$  is the smallest norm  $\|\cdot\|_M$  of a non-zero vector in the grid  $\mathbb{Z}^2$ :

$$\lambda_1(M) := \min_{e \in \mathbb{Z}^2 \setminus \{0\}} \|e\|_M. \quad (8)$$

Denoting by  $e$  a minimizer in the above expression, the second Minkowski minimum is the smallest norm  $\|\cdot\|_M$  of an element of  $\mathbb{Z}^2$  non-collinear to  $e$ :

$$\lambda_2(M) := \min_{f \in \mathbb{Z}^2 \setminus e\mathbb{Z}} \|f\|_M. \quad (9)$$

A  $M$ -reduced basis is a pair  $(e, f)$  of minimizers of (8) and (9). Simple arguments of linear algebra [9] show that the value  $\lambda_2(M)$  does not depend on the choice of the minimizer  $e$  of (8), and that a  $M$ -reduced basis is automatically a basis of  $\mathbb{Z}^2$ , in the sense of (7). We emphasize that obtaining a  $M$ -reduced basis, i.e. solving the minimization problems (8) and (9), is both simple and cheap numerically. This is the object of Gauss's algorithm [9]: initialize  $(e, f)$  as the canonical basis of  $\mathbb{Z}^2$ , and

$$\begin{aligned} &\text{Do } (e, f) := (f, e - \text{Round}(\langle e, Mf \rangle / \|f\|_M^2) f), \quad (10) \\ &\text{while } \|e\|_M > \|f\|_M. \end{aligned}$$

The number of iterations is  $\mathcal{O}(\ln \kappa(M))$ , logarithmic in the anisotropy ratio  $\kappa(M)$  of the matrix  $M$ , which is defined by

$$\kappa(M) := \sqrt{\|M\| \|M^{-1}\|} = \max_{\|u\|=\|v\|=1} \frac{\|u\|_M}{\|v\|_M}.$$

The elements  $e, f$ , of a  $M$ -reduced basis, are heuristically never very far from being orthogonal, with respect to the scalar product  $\langle \cdot, M \cdot \rangle$ . Indeed, since  $f$  minimizes  $\|\cdot\|_M$  among elements of  $\mathbb{Z}^2$  non collinear to  $e$ , we have  $\|f\|_M \leq \|f - e\|_M$  and  $\|f\|_M \leq \|f + e\|_M$ . Squaring these inequalities, we obtain

$$2|\langle e, Mf \rangle| \leq \|e\|_M^2. \quad (11)$$

Assume that  $\langle e, Mf \rangle \leq 0$ , up to replacing  $f$  with  $-f$ , and define  $g := -e - f$ . We obtain

$$\begin{aligned} \langle f, Mg \rangle &= -\langle e, Mf \rangle - \|f\|_M^2 \leq -\frac{1}{2}\|f\|_M^2 < 0, \quad (12) \\ \langle g, Me \rangle &= -\langle e, Mf \rangle - \|e\|_M^2 \leq -\frac{1}{2}\|e\|_M^2 < 0. \end{aligned}$$

If  $M = \mathbf{M}(z)$ , then we define the weights  $\gamma_z$  in the AD-LBR (3), by

$$\gamma_z(\pm e) := -\langle f, Mg \rangle / (2 \det M), \quad (13)$$

and likewise permuting circularly the roles of  $e, f, g$ . The map  $\gamma_z : \mathbb{Z}^2 \rightarrow \mathbb{R}_+$  is non-negative, even, identically zero except at  $e, f$ , perhaps  $g$ , and their opposites. See Figure 1. We show in lemma 8 that  $\gamma_z$  is independent of the choice of  $M$ -reduced basis  $(e, f)$ . In view of Lemma 1, we just constructed the decomposition (5) of  $\mathbf{D}(z) = \mathbf{M}(z)^{-1} = M^{-1}$ , with non-negative coefficients as desired.

A 3D extension of this construction is proposed in §2. The proof is partly computer assisted, as it involves solving a  $21 \times 21$  linear system (explicit and with integer entries) which solution is checked to be non-negative. The construction has a similar cost  $\mathcal{O}(\ln \kappa(M))$ .

The AD-LBR energy  $\mathcal{E}_h : L^2(\Omega_h) \rightarrow \mathbb{R}_+$ , see (3), is written in terms of the above constructed coefficients  $\gamma_z$ , and of stencils  $V(z) \subset \mathbb{Z}^2$ , defined as follows. For each  $z \in \Omega$ , we set

$$V(z) := \{e \in \mathbb{Z}^d; \gamma_z(e) \neq 0\}, \quad (14)$$

in the case of periodic or reflected boundary conditions on a rectangular domain, and in the case of Dirichlet boundary conditions on a general domain (extending  $u$  by zero outside  $\Omega_h$ ). In the case of Neumann boundary conditions on a general domain, one should set

$$V(z; h) := \{e \in \mathbb{Z}^d; \gamma_z(e) \neq 0 \text{ and } z + he \in \Omega_h\}.$$

We have so far established three strongpoints of the AD-LBR:

**Non-negativity.** Off diagonal coefficients of the symmetric semi-definite  $N \times N$  matrix,  $N = \#(\Omega_h)$ , associated to the energy  $\mathcal{E}_h$  are non-positive, while diagonal coefficients are positive.

**Sparsity.** Stencil size is uniformly bounded, independently of the anisotropy of the diffusion tensor:  $\#(V(z)) \leq 6$  in 2D, and  $\#(V(z)) \leq 14$  in 3D, for all  $z \in \Omega$ .

**Complexity.** The construction of the stencil  $V(z)$ , and of the associated coefficients  $\gamma_z$ , has a logarithmic cost  $\mathcal{O}(\ln \kappa(\mathbf{D}(z)))$  in the anisotropy ratio of the diffusion tensor.

The next result, Theorem 1, restricted to the two dimensional case, establishes that AD-LBR is asymptotically equivalent to a more involved and computationally intensive procedure: a finite element discretization of the energy (1), on an *Anisotropic Delaunay Triangulation* (ADT, see [5] and below) of the domain  $\Omega$ . Under the assumptions of this theorem, AD-LBR benefits from two additional guarantees, that we state informally and without proof.

**No chessboard artifacts.** Some numerical schemes for anisotropic diffusion suffer from chessboard artifacts, in the sense that periodic artifacts develop at the pixel level. Such artifacts cannot develop in finite element discretizations, since they would lead to high frequency oscillations of the finite element interpolant, and therefore to an increase of the energy (15). The asymptotic equivalence of the AD-LBR with a finite element discretization also rules out these defects.

**Spectral correctness.** The  $n$ -th smallest eigenvalue  $\lambda_n(h)$  of the symmetric matrix associated to  $h^{-d}\mathcal{E}_h$  (3), converges as  $h \rightarrow 0$  towards the  $n$ -th smallest eigenvalue  $\lambda_n$  of the continuous operator  $-\operatorname{div}(\mathbf{D}\nabla)$ , for any given integer  $n \geq 0$ . This follows from a similar property of the finite element energy  $\mathcal{E}'_h$  (15), and from the asymptotic equivalence (16).

Our convergence result, Theorem 1 below, is specialized to the case of a square periodic domain, which covers reflecting boundary conditions frequently used in image processing. Since the grid discretization must be compatible with the boundary conditions, any scale parameter  $h$  appearing in the rest of the paper is assumed to be the inverse of a positive integer:

$$h \in \{1/n; n \geq 1\}.$$

**Theorem 1.** *Let  $\Omega$  be the unit square  $[0, 1]^2$ , equipped with periodic boundary conditions. Let  $\mathbf{D} : \bar{\Omega} \rightarrow S_2^+$  be a (periodic) diffusion tensor with Lipschitz regularity, and let  $\mathbf{M} := \mathbf{D}^{-1}$ . When  $h$  is sufficiently small, the periodic Riemannian domain  $(\Omega, \mathbf{M})$  admits an Anisotropic Delaunay Triangulation  $\mathcal{T}_h$ , with collection of vertices  $\Omega_h := \Omega \cap h\mathbb{Z}^2$ . For  $u \in L^2(\Omega_h)$ , define*

$$\mathcal{E}'_h(u) := \int_{\Omega} \|\nabla(\mathbf{I}_{\mathcal{T}_h} u)(z)\|_{\mathbf{D}(z)}^2 dz, \quad (15)$$

where  $\mathbf{I}_{\mathcal{T}}$  denotes the piecewise linear interpolation operator on a triangulation  $\mathcal{T}$ . Then for some constant  $c = c(\mathbf{D})$ , independent of  $u$  and  $h$ ,

$$(1 - ch)\mathcal{E}_h(u) \leq \mathcal{E}'_h(u) \leq (1 + ch)\mathcal{E}_h(u). \quad (16)$$

The proof of this result is postponed to §3, but for the sake of concreteness, we describe the concept of

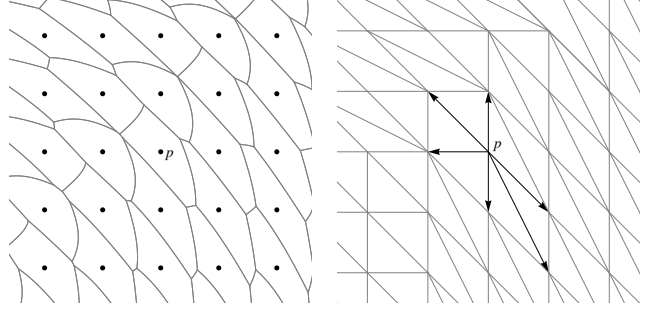


Figure 2: Construction of an Anisotropic Delaunay Triangulation. Left: the grid points  $p \in \Omega_h$ , and the Voronoi cells  $\operatorname{Vor}_h(p)$ . Right: the triangulation  $\mathcal{T}_h$ , obtained (generically) by connecting grid points which Voronoi cells intersect. The stencil  $V_h(p)$  is represented by arrows. (In order to handle the non generic cases where four or more Voronoi regions intersect at the same point, an intermediate polygonization  $Q_h$  is introduced in the text.)

Anisotropic Delaunay Triangulation (ADT) [5]. In the rest of this introduction, and in §3, we assume as in Theorem 1 that the diffusion tensor  $\mathbf{D}$  is defined on the square  $[0, 1]^2$  and satisfies periodic boundary conditions. We extend it, as well as its inverse the metric  $\mathbf{M}$ , to the whole plane  $\mathbb{R}^2$  by periodicity.

We specialize the concept of ADT [5], to the domain  $\mathbb{R}^2$  and the collection of vertices  $h\mathbb{Z}^2$ . For that purpose, we introduce some notations. For all  $p, q \in \mathbb{R}^2$ , we denote by  $\delta_p(q)$  the distance from  $p$  to  $q$ , as measured by the metric at the point  $p$ :

$$\delta_p(q) := \|q - p\|_{\mathbf{M}(p)}.$$

We denote by  $\Delta_h(q)$  the least distance from a point  $q \in \mathbb{R}^2$ , to the grid  $h\mathbb{Z}^2$ :

$$\Delta_h(q) := \min_{p \in h\mathbb{Z}^2} \delta_p(q). \quad (17)$$

We introduce the Voronoi cell  $\operatorname{Vor}_h(p)$  of a grid point  $p \in h\mathbb{Z}^2$ , which is the collection of points  $q \in \mathbb{R}^2$  closer to  $p$  than to any other grid point:

$$\operatorname{Vor}_h(p) := \{q \in \mathbb{R}^2; \delta_p(q) = \Delta_h(q)\}. \quad (18)$$

The collection of Voronoi cells is referred to as the Voronoi diagram, see Figure 2 (left). A Voronoi vertex is a point  $q \in \mathbb{R}^2$  at which at least three distinct Voronoi regions intersect:  $(\operatorname{Vor}_h(p_i))_{i=1}^k$ ,  $k \geq 3$ ,  $p_i \in h\mathbb{Z}^2$ . We attach to  $q$  a dual Voronoi cell  $T_q$ , defined as the convex hull of the points  $(p_i)_{i=1}^k$ .

The geometric dual  $\mathcal{Q}_h$ , of the Voronoi diagram, is defined as the collection of all dual Voronoi cells  $T_q$ . Note that, generically on the metric  $\mathbf{M}$ , no more than three Voronoi regions can intersect at any point in  $\mathbb{R}^2$ , thus

the elements of  $\mathcal{Q}_h$  are generically triangles. If  $h$  is small enough, we show in §3 (using the Dual Triangulation Theorem in [5]) that  $T_q$  is a strictly convex polygon, of vertices  $(p_i)_{i=1}^k$  with the above notations, and that  $\mathcal{Q}_h$  is a polygonization (generically a triangulation) of  $\mathbb{R}^2$ , with vertices  $h\mathbb{Z}^2$ .

Since the metric  $\mathbf{M}$  and the vertices  $h\mathbb{Z}^2$  are periodic (recall that  $h = 1/n$  for some integer  $n \geq 1$ ), arbitrarily triangulating the elements of  $\mathcal{Q}_h$ , respecting periodicity, yields a periodic triangulation  $\mathcal{T}_h$ .

**Definition 1** (ADT, Labelle and Shewchuk [5]). *The triangulation  $\mathcal{T}_h$  obtained by the above construction is referred to as an ADT of the domain  $\mathbb{R}^2$ , with collection of vertices  $h\mathbb{Z}^2$ , and underlying Riemannian metric  $\mathbf{M}$ . Since  $\mathcal{T}_h$  is  $\mathbb{Z}^2$ -periodic, we also regard it as an ADT of the periodic unit square  $\Omega$ .*

We establish in §3.1 the existence of the ADT  $\mathcal{T}_h$ . Subsection §3.2 is devoted to the study of reduced bases: their characterization, uniqueness and stability properties. We study in §3.3 the finite element stencils, defined for  $p \in h\mathbb{Z}^2$  by

$$V_h(p) := \{e \in \mathbb{Z}^2; [p, p + he] \text{ is an edge of } \mathcal{T}_h\}. \quad (19)$$

See Figure 2 (right). We show that  $V_h(p)$  coincides with the AD-LBR stencil  $V(p)$ , unless the lattice  $\mathbb{Z}^2$  admits a basis *almost orthogonal* with respect to the scalar product associated to  $\mathbf{M}(p)$ , see Lemma 10. This is tied to the fact that orthogonal grids admit several (usual) Delaunay triangulations. Overcoming this technical difficulty, we conclude the proof of Theorem 1.

Note that the construction of the ADT  $\mathcal{T}_h$  is not easy to parallelize, in particular when anisotropy is pronounced since the Voronoï regions of far away points interact. The construction of  $\mathcal{T}_h$  also involves solving polynomial equations of degree four, because Voronoï regions boundaries are conics, and Voronoï vertices must be identified at their intersections. In contrast, the stencils of the AD-LBR are independent of each other, and their construction is essentially contained in the two lines program (10).

## 2 Three dimensional stencils

We construct in this section the 3D stencils of the AD-LBR. We also discuss in Remark 1 the euclidean radius of these stencils, in 2D and 3D.

We denote by  $e_1\mathbb{Z} + \dots + e_k\mathbb{Z}$  the sub-lattice of  $\mathbb{Z}^d$  generated by vectors  $e_1, \dots, e_k \in \mathbb{Z}^d$ . This sub-lattice equals  $\{0\}$  by convention if  $k = 0$ . We say that  $(e_1, \dots, e_d) \in (\mathbb{Z}^d)^d$  is a basis of  $\mathbb{Z}^d$  if  $e_1\mathbb{Z} + \dots + e_d\mathbb{Z} = \mathbb{Z}^d$ , or equivalently if

$$|\det(e_1, \dots, e_d)| = 1.$$

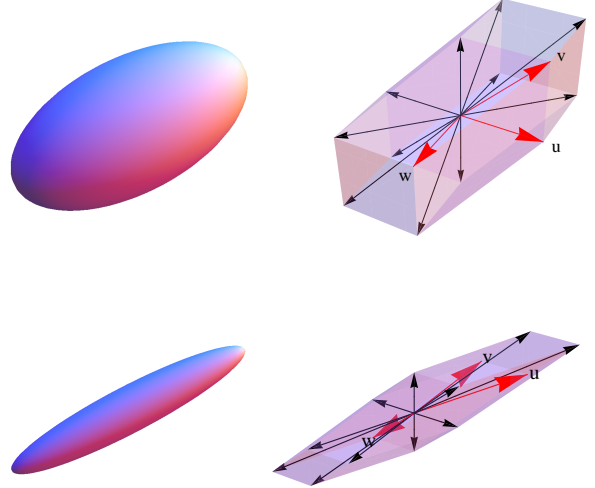


Figure 3: Right: stencil of the AD-LBR, for a symmetric matrix of eigenvector  $M$  of anisotropy ratio  $\kappa(M)$  equal to 2 (top) or 6 (bottom). The anisotropy is of “needle” type: the two largest eigenvalues of  $M$  are equal, and the needle orientation is given by the vector  $(4, 2, 3)$ . The ellipsoid  $\{z \in \mathbb{R}^3; \|z\| \leq 1\}$  is shown left.

**Definition 2.** *Given  $M \in S_d^+$ ,  $d \leq 4$ , we say that a basis  $(e_1, \dots, e_d)$  of  $\mathbb{Z}^d$  is a  $M$ -reduced basis if for all  $1 \leq i \leq d$*

$$\|e_i\|_M \in \operatorname{argmin}\{\|e\|_M; e \in \mathbb{Z}^d \setminus (e_1\mathbb{Z} + \dots + e_{i-1}\mathbb{Z})\}.$$

There always exists a  $M$ -reduced basis in dimension  $d \leq 4$ , see [9]. The norms

$$\lambda_i(M) := \|e_i\|_M, \quad (20)$$

of the elements  $(e_i)_{i=1}^d$  of a  $M$ -reduced basis, are called the Minkowski minima, and are independent of the choice of  $M$ -reduced basis. Such bases can be obtained via a generalization of Gauss’s algorithm (10), still of complexity  $\mathcal{O}(\ln \kappa(M))$ , see [9] for the proof, and Theorem 1.5 in [6] for a discussion. In dimension  $d \geq 5$  there may not exist any  $M$ -reduced basis in the sense of Definition 2, and the relevant notion is Minkowski reduction [9].

The AD-LBR, three dimensional, 14 element symmetric stencil  $V(z)$  is obtained by symmetrizing the 7 element stencil  $\mathcal{V}$  described in the next theorem, for  $M := \mathbf{M}(z)$ . This stencil was originally designed for solving 3D static Hamilton Jacobi (HJ) PDEs in [6]. It is not yet clear whether the 4D stencil proposed in [7] for HJ PDEs, can be used to extend the AD-LBR to four dimensions.

**Theorem 2.** *Let  $M \in S_3^+$ , and let  $(e_1, e_2, e_3)$  be a  $M$ -reduced basis. Let  $u := \pm e_{\sigma(1)}$ ,  $v := \pm e_{\sigma(2)}$ , and*

$w = \pm e_{\sigma(3)}$ , where the permutation  $\sigma$  of  $\{1, 2, 3\}$  is such that  $|\langle v, Mw \rangle| \geq |\langle u, Mv \rangle| \geq |\langle u, Mw \rangle|$ , and the signs are chosen so that  $\langle u, Mv \rangle \geq 0$  and  $\langle u, Mw \rangle \geq 0$ . Thus

$$|\langle v, Mw \rangle| \geq \langle u, Mv \rangle \geq \langle u, Mw \rangle \geq 0. \quad (21)$$

Then there exists a 7 element family  $\mathcal{V} = (e_i)_{i=1}^7$ , and non-negative coefficients  $(\gamma_i)_{i=1}^7$ , such that

$$M^{-1} = \sum_{1 \leq i \leq 7} \gamma_i e_i e_i^T.$$

(n) If  $\langle v, Mw \rangle \leq 0$ , then

$$\mathcal{V} := (u, v, w, u - v, u - w, v + w, u - v - w).$$

(p) If  $\langle v, Mw \rangle > 0$ , then

$$\mathcal{V} := (u, v, w, u - v, u - w, v - w, u - v + w).$$

*Proof.* Let  $A$  be the  $3 \times 3$  matrix which columns are  $(u, v, w)$ . We assume, up to replacing  $M$  with  $A^T M A$ , that  $(u, v, w)$  is the canonical basis of  $\mathbb{R}^3$ .

We denote by  $u \cdot v$  the scalar product  $\langle u, Mv \rangle$ , and by  $u^2$  the squared norm  $\|u\|_M^2 = \langle u, Mu \rangle = u \cdot u$ . Recall that the inverse of  $M$  is positively proportional to its comatrix  $\hat{M} := \det(M) M^{-1}$ . The coefficients  $(\hat{M}_{ij})_{i,j=1}^3$  of the comatrix are  $2 \times 2$  minors of  $M$ , hence quadratic forms in its coefficients  $(M_{ij})_{i,j=1}^3$ . For instance, recalling that  $(u, v, w)$  is here assumed to be the canonical basis of  $\mathbb{R}^3$ :

$$\hat{M}_{11} = M_{22}M_{33} - M_{23}M_{32} = v^2w^2 - (v \cdot w)^2.$$

$$\hat{M}_{21} = M_{32}M_{13} - M_{12}M_{33} = (v \cdot w)(u \cdot w) - (u \cdot v)w^2.$$

The rank 1 symmetric matrices  $zz^T$ , where  $z$  ranges over the six first elements of  $\mathcal{V}$ , are easily checked to be a basis of six dimensional space of  $3 \times 3$  symmetric matrices. The vector  $\alpha \in \mathbb{R}^6$  of the coefficients of  $\hat{M}$  on this basis is given below in case (n):

$$\alpha := (\hat{M}_{11} + \hat{M}_{12} + \hat{M}_{13}, \hat{M}_{21} + \hat{M}_{22} - \hat{M}_{23}, \hat{M}_{31} - \hat{M}_{32} + \hat{M}_{33}, -\hat{M}_{12}, -\hat{M}_{13}, \hat{M}_{23}).$$

In case (p), replace  $\hat{M}_{23}$  with  $-\hat{M}_{23}$  (and  $\hat{M}_{32}$  with  $-\hat{M}_{32}$ ) in the above expression of  $\alpha$ . The rank one matrix  $zz^T$ , where  $z$  is the last element of the stencil  $\mathcal{V}$ , can also be decomposed on this basis, with coefficient vector  $\beta := (-1, -1, -1, 1, 1, 1)$  in case (n) (resp.  $\beta := (1, -1, 1, 1, -1, 1)$  in case (p)).

As a result, we can write the comatrix  $\hat{M}$  as the linear sum of  $zz^T$ , where  $z$  ranges over  $\mathcal{V}$ , with coefficient vector  $(\alpha - t\beta, t) \in \mathbb{R}^7$ , for any  $t \in \mathbb{R}$ . The proof of Theorem 2 will be complete when we find  $t \in \mathbb{R}_+$ , such that  $\alpha - t\beta \in \mathbb{R}_+^6$ .

Such a value of  $t$  will satisfy  $t \leq \alpha_i$  for each  $1 \leq i \leq 6$  such that  $\beta_i = 1$ , and  $t \geq -\alpha_j$  for each  $j$  such that  $\beta_j =$

$-1$ . We denoted by  $(\alpha_i)_{i=1}^6$  and  $(\beta_i)_{i=1}^6$  the coefficients of  $\alpha$  and  $\beta$ . The range of admissible values of  $t$  is thus

$$\max\{0, \max\{-\alpha_j; \beta_j = -1\}\} \leq t \leq \min\{\alpha_i; \beta_i = 1\}.$$

If this range is non-empty, then  $\alpha_i + \alpha_j \geq 0$  whenever  $\beta_i\beta_j = -1$ , and  $\alpha_i \geq 0$  whenever  $\beta_i = 1$ . Conversely, if these inequalities are satisfied, then the range of admissible  $t$  is non-empty, and Theorem 2 is proved.

We thus only have to prove the non-negativity of a finite number, twelve in each case to be exact, of quadratic forms  $(\alpha_i, \text{ or } \alpha_i + \alpha_j, \text{ for the values of } i, j \text{ given above})$  in the quantities  $(u^2, v^2, w^2, u \cdot v, u \cdot w, v \cdot w)$ . We know that the six following linear forms of these quantities are non-negative:

- In case (n):  $u \cdot w, u \cdot v - u \cdot w, -v \cdot w - u \cdot v,$  and  $u^2 - 2u \cdot v, v^2 + 2v \cdot w, w^2 + 2v \cdot w.$
- In case (p):  $u \cdot w, u \cdot v - u \cdot w, v \cdot w - u \cdot v,$  and  $u^2 - 2u \cdot v, v^2 - 2v \cdot w, w^2 - 2v \cdot w.$

In each case, the three first follow from (21), and the three last are obtained as in (11) (use the fact that  $\|e_i \pm e_j\|_M \geq \|e_i\|_M$  for any distinct  $i, j$ ). Multiplying these six linear forms by one another, we obtain 21 distinct quadratic forms which take non-negative values, and happen to be a basis of the 21-dimensional vector space of quadratic forms over the six variables  $(u^2, v^2, w^2, u \cdot v, u \cdot w, v \cdot w)$ . It also happens that the coefficients of the 12 of quadratic forms interest  $(\alpha_i \text{ or } \alpha_i + \alpha_j, \text{ see above})$  on this basis are non-negative; this is shown by inverting a  $21 \times 21$  explicit matrix with integer entries, see the ancillary file. Hence they take non-negative values, which concludes the proof.  $\square$

**Remark 1** (Stencil radius). Consider a matrix  $M \in S_d^+$ , where  $d \in \{2, 3\}$ , and the associated stencil  $V$  used in the AD-LBR. As discussed in the introduction, the stencil cardinality  $\#(V)$  has a direct impact on the scheme complexity, and is hopefully bounded independently of  $M$ : by 6 in 2D, and by 14 in 3D. The stencil euclidean radius

$$r := \max\{\|v\|; v \in V\}$$

can however also have an indirect impact on computation time. A large radius may e.g. provoke non-local memory accesses and cache misses, which can raise crucial issues in the prospect of a GPU implementation.

Observe that, for any  $e \in \mathbb{R}^d$

$$\|e\| \|M^{-1}\|^{-\frac{1}{2}} \leq \|e\|_M \leq \|e\| \|M\|^{\frac{1}{2}} \quad (22)$$

Thus, in view of the stencil construction,

$$r \leq d\lambda_d(M) \|M^{-1}\|^{\frac{1}{2}}. \quad (23)$$

Inequality (22) also implies

$$\|M^{-1}\|^{-\frac{1}{2}} \leq \lambda_1(M) \leq \dots \leq \lambda_d(M) \leq \|M\|^{\frac{1}{2}}, \quad (24)$$

see e.g. Proposition 1.6 in [6]. Combining (23) and (24), we obtain the worst case upper bound  $r \leq d\kappa(M)$ .

An average case estimate of  $\lambda_d$  is proved in [7]. Denoting by  $\mathcal{O}_d$  the group of rotations of  $\mathbb{R}^d$ , equipped with the Haar measure:

$$\int_{\mathcal{O}_d} \lambda_d(R^T M R) dR \leq C_d \det(M)^{\frac{1}{2d}}. \quad (25)$$

Let  $\bar{r}$  be the average value, over grid orientations, of the stencil radius. Combining (23) and (25) we obtain, in two dimensions, the estimate  $\bar{r} \leq 2C_2 \sqrt{\kappa(M)}$ .

### 3 Equivalence to a finite element discretization

This section is devoted to the proof Theorem 1: the asymptotic equivalence of AD-LBR with a finite element discretization. We use the notations of §1. The existence of the ADT  $\mathcal{T}_h$  is established in the first subsection, for  $h$  sufficiently small, as well as a few of its properties. The second subsection is devoted to the study of  $M$ -reduced bases. Theorem 1 is proved in the third subsection, by comparing the stencils of the AD-LBR and of the finite element discretization.

#### 3.1 Existence of an ADT

We introduce three positive reals  $\nu_1, \nu_2, \nu_{\div}$ , defined by

$$\begin{aligned} \nu_1 &:= \min\{\|\mathbf{M}(z)^{-1}\|^{-\frac{1}{2}}; z \in \mathbb{R}^2\}, \\ \nu_2 &:= \max\{\|\mathbf{M}(z)\|^{\frac{1}{2}}; z \in \mathbb{R}^2\}, \\ \nu_{\div} &:= \frac{\nu_2}{\nu_1}. \end{aligned} \quad (26)$$

Thus for all  $p, r \in \mathbb{R}^2$

$$\nu_1 \|p - r\| \leq \delta_p(r) := \|p - r\|_{\mathbf{M}(p)} \leq \nu_2 \|p - r\|. \quad (27)$$

**Lemma 2.** • For all  $r \in \mathbb{R}^2$ , one has  $\Delta_h(r) \leq \nu_2 h$ .

- If  $p, q \in h\mathbb{Z}^2$ , and  $r \in \text{Vor}_h(p) \cap \text{Vor}_h(q)$ , then  $\|p - r\| \leq \nu_{\div} h$  and  $\|p - q\| \leq 2\nu_{\div} h$ .

*Proof.* First point. Rounding the coordinates of  $r$  to a nearest multiple of  $h$ , we obtain a point  $p \in h\mathbb{Z}^2$  such that  $\|p - r\| \leq h$ . Recalling (27) we obtain  $\delta_p(r) \leq \nu_2 h$ , and therefore  $\Delta_h(r) \leq \nu_2 h$  in view of (17).

Second point. We have  $\nu_1 \|p - r\| \leq \delta_p(r) = \Delta_h(r) \leq \nu_2 h$ . Thus  $\|p - r\| \leq \nu_{\div} h$ , and likewise  $\|q - r\| \leq \nu_{\div} h$ . Finally, by the triangle inequality,  $\|p - q\| \leq \|p - r\| + \|q - r\| \leq 2\nu_{\div} h$ .  $\square$

Following the notations of [5], we denote by  $\tau(p, q)$ ,  $p, q \in \mathbb{R}^2$ , the smallest constant  $\tau \geq 1$  such that

$$\tau^{-1} \delta_p(r) \leq \delta_q(r) \leq \tau \delta_p(r), \quad \text{for all } r \in \mathbb{R}^2.$$

Equivalently, in the sense of symmetric matrices,

$$\tau^{-2} \mathbf{M}(p) \leq \mathbf{M}(q) \leq \tau^2 \mathbf{M}(p). \quad (28)$$

We also define a quantity  $\tau_h \geq 1$ , closely related to the modulus of continuity of the metric  $\mathbf{M}$ :

$$\tau_h := \max\{\tau(p, q); \|p - q\| \leq 2\nu_{\div} h\}. \quad (29)$$

One has  $\tau_h \rightarrow 1$  as  $h \rightarrow 0$ , for any continuous metric  $\mathbf{M}$  (indeed  $\mathbf{M}$  is periodic and therefore uniformly continuous). If  $\mathbf{M}$  is Lipschitz, as assumed in Theorem 1, then  $\tau_h = 1 + \mathcal{O}(h)$ .

We assume, in the rest of this subsection, that  $h$  is sufficiently small so that

$$\tau_h < \sqrt{1 + \nu_{\div}^{-2}}. \quad (30)$$

**Lemma 3.** • If  $p, q \in h\mathbb{Z}^2$ ,  $p \neq q$ , and  $r \in \text{Vor}_h(p) \cap \text{Vor}_h(q)$ , then  $\delta_p(r) < \delta_p(q) / \sqrt{\tau(p, q)^2 - 1}$ .

- The geometric dual  $\mathcal{Q}_h$  of the Voronoï diagram is, as announced in §1, a polygonization of  $\mathbb{R}^2$  into strictly convex polygons, with vertices  $h\mathbb{Z}^2$ .

*Proof.* First point. We may assume that  $\tau(p, q) > 1$ , otherwise there is nothing to prove. The second point of Lemma 2 implies that  $\|p - q\| \leq 2\nu_{\div} h$ , thus

$$\sqrt{\tau(p, q)^2 - 1} \leq \sqrt{\tau_h^2 - 1} < 1/\nu_{\div}.$$

On the other hand  $\delta_p(q) \geq \nu_1 \|q - p\| \geq \nu_1 h$ , and  $\delta_p(r) \leq \Delta_h(r) \leq \nu_2 h$ . The announced inequality follows.

Second point. We apply Theorem 7 (Dual Triangulation Theorem) in [5]. Since the domain  $\mathbb{R}^2$  has no boundary, it suffices to check that all the Voronoï arcs and vertices are *wedged*, see [5]. This condition means that for any  $p, q \in h\mathbb{Z}^2$  such that  $p \neq q$ , and any  $r \in \text{Vor}_h(p) \cap \text{Vor}_h(q)$ , one has  $(r - q) \mathbf{M}(q)(p - q) > 0$ , and likewise exchanging the roles of  $p$  and  $q$ . Heuristically, it expresses the acuteness of some angles measured in the local metric. Lemma 5 in [5] shows that this condition follows from the first point of this lemma, which concludes the proof.  $\square$

We recall that  $\mathcal{T}_h$  is the triangulation obtained by arbitrarily triangulating the polygonization  $Q_h$  of the previous lemma, respecting periodicity, see Definition 1. Generically  $Q_h$  is already a triangulation, hence  $\mathcal{T}_h = Q_h$ , see §1.

We establish in the next lemma a few properties of the elements of  $\mathcal{T}_h$ . Note that the vertices  $p, q, r$  of any triangle  $T \in \mathcal{T}_h$  satisfy by construction

$$\text{Vor}_h(p) \cap \text{Vor}_h(q) \cap \text{Vor}_h(r) \neq \emptyset. \quad (31)$$

The Voronoï regions  $\text{Vor}_h$ , and the triangulation  $\mathcal{T}_h$  are illustrated on Figure 2.

**Lemma 4.** Denote by  $he, hf, hg$  the edges of a triangle  $T \in \mathcal{T}_h$ , where  $e, f, g \in \mathbb{Z}^2$  are oriented so that  $e+f+g=0$ . Then

**Diameter:**  $\max\{\|e\|, \|f\|, \|g\|\} \leq 2\nu_{\div}$ .

**Area:**  $|\det(e, f)| = 1$ , thus  $|T| = h^2/2$ .

**Acuteness:**  $\langle e, \mathbf{M}(z)f \rangle \leq \theta_h$ , for any  $z \in T$ , where  $\theta_h := \nu_{\div}^2(3 + 9\tau_{2h}^2)(\tau_{2h}^2 - 1)$ .

*Proof.* First point. We denote by  $p, q, r$  the vertices of  $T$ , ordered in such way that  $p+he = q, q+hf = r, r+hg = p$ . The announced estimate follows from (31), and from the second point of Lemma 2.

Second point. Since  $\mathcal{T}_h$  is a conforming triangulation, the intersection of  $T$  with the collection  $h\mathbb{Z}^2$  of all vertices of  $\mathcal{T}_h$  consists of only three points: the vertices  $p, q, r$  of  $T$ . Thus the triangle of vertices  $-e, 0, f$ , homothetic to  $T$ , contains no point of integer coordinates but its vertices. This implies that  $(e, f)$  is a basis of  $\mathbb{Z}^2$ , hence  $|\det(e, f)| = 1$ , as announced.

Third point. The pairwise distances between  $p, q, r$  are bounded by  $2\nu_{\div}h$  (first point), and since  $z \in T$  so are the pairwise distances between  $p, q, r, z$ . Defining  $s := p - q + r \in h\mathbb{Z}^2$ , and observing that  $\|s - p\| = \|r - q\| \leq 2\nu_{\div}h$ , we find that the pairwise distances between  $p, q, r, z, s$  are bounded by  $4\nu_{\div}h$ .

Let  $x \in \text{Vor}_h(p) \cap \text{Vor}_h(q) \cap \text{Vor}_h(r)$ . We have  $\delta_p(x) = \delta_q(x) = \delta_r(x) = \Delta_h(x) \leq \delta_s(x)$ , thus

$$\delta_s(x)^2 \geq \delta_p(x)^2 - \delta_q(x)^2 + \delta_r(x)^2. \quad (32)$$

(For intuition: in a classical Delaunay triangulation,  $x$  would be the circumcenter of  $T$ , and (32) state that  $s$  is outside the circumcircle.) Denoting  $M := \mathbf{M}(z)$ , and  $\delta := \Delta_h(x)$ , we obtain

$$\begin{aligned} |\delta_p(x)^2 - \|x - p\|_M^2| &\leq \delta_p(x)^2(\tau(p, z)^2 - 1) \\ &\leq \delta^2(\tau_{2h}^2 - 1), \end{aligned} \quad (33)$$

using Lemma 2, and likewise for  $q, r$ . We also have

$$\begin{aligned} \delta_s(x) &= \|p - q + r - x\|_{\mathbf{M}(s)} \\ &\leq \|p - x\|_{\mathbf{M}(s)} + \|q - x\|_{\mathbf{M}(s)} + \|r - x\|_{\mathbf{M}(s)} \\ &\leq 3\delta\tau_{2h}. \end{aligned}$$

Thus, proceeding as in (33),

$$|\delta_s(x) - \|s - x\|_M^2| \leq \delta_s(x)^2(\tau_{2h}^2 - 1) \leq 9\delta^2\tau_{2h}^2(\tau_{2h}^2 - 1).$$

Injecting in (32) these estimates of  $\delta_{\star}(x)$ ,  $\star \in \{p, q, r, s\}$ , and using the fact that  $\delta \leq h\nu_2$ , see Lemma 2, we obtain after expansion the announced estimate of  $\langle e, Mf \rangle$ .  $\square$

We next rewrite the finite element energy  $\mathcal{E}'_h$  (15) in a form that can be easily compared with the AD-LBR

energy  $\mathcal{E}_h$  (3), which is written in terms of coefficients  $\gamma_p$  and stencils  $V(p)$ ,  $p \in \Omega_h$ .

We denote by  $\varphi_p^h : \mathbb{R}^2 \rightarrow \mathbb{R}$  the piecewise linear function on  $\mathcal{T}_h$  such that  $\varphi_p^h(p) = 1$ , and  $\varphi_p^h(q) = 0$  for any vertex  $q \in h\mathbb{Z}^2$  distinct from  $p$ . This is the classical ‘‘hat function’’ encountered in finite element analysis. For all  $p \in h\mathbb{Z}^2$ ,  $e \in \mathbb{Z}^2$ , we define

$$\gamma_p^h(e) := -\frac{1}{2} \int_{\mathbb{R}^2} \langle \nabla \varphi_p^h(z), \mathbf{D}(z) \nabla \varphi_{p+he}^h(z) \rangle dz \quad (34)$$

Clearly,  $\gamma_p^h(e) = 0$  if  $[p, p+he]$  is not an edge of  $\mathcal{T}_h$ , in other words if  $e$  does not belong to the stencil  $V_h(p)$ , defined in (19). We express in the next lemma the finite element energy  $\mathcal{E}'_h$  (15), in terms of the stencils  $V_h$  and of the (potentially negative) weights  $\gamma_p^h$ .

**Lemma 5.** For any  $u \in L^2(\Omega_h)$ , extended by periodicity to  $h\mathbb{Z}^2$ , one has

$$\mathcal{E}'_h(u) = \sum_{p \in \Omega_h} \sum_{e \in V_h(p)} \gamma_p^h(e) |u(p+he) - u(p)|^2. \quad (35)$$

*Proof.* For any triangle  $T \in \mathcal{T}_h$ , and any  $p, q \in h\mathbb{Z}^2$ , we denote

$$s_T(p, q) := \int_T \langle \nabla \varphi_p^h(z), \mathbf{D}(z) \nabla \varphi_q^h(z) \rangle dz.$$

Clearly  $s_T(p, q) = 0$  if  $q$  or  $p$  is not a vertex of  $T$ . The coefficient  $\gamma_p^h(e)$ ,  $e \in \mathbb{Z}^2$ , is thus given by the following sum with at most two non-zero terms:

$$\gamma_p^h(e) = -\frac{1}{2} \sum_{T \in \mathcal{T}_h} s_T(p, p+he). \quad (36)$$

Let  $p, q, r \in h\mathbb{Z}^2$  be the vertices of a triangle  $T \in \mathcal{T}_h$ . Since the sum  $\varphi_p^h + \varphi_q^h + \varphi_r^h$  is constant on  $T$ , equal to 1, it has a null gradient on  $T$ , and therefore

$$s_T(p, p) + s_T(p, q) + s_T(p, r) = 0.$$

Using this relation, and the two similar ones obtained by permuting circularly  $p, q, r$ , we obtain

$$\begin{aligned} &\int_T \|\nabla(\mathbf{I}_{\mathcal{T}_h} u)(z)\|_{\mathbf{D}(z)}^2 dz \\ &= u(p)^2 s_T(p, p) + u(q)^2 s_T(q, q) + u(r)^2 s_T(r, r) \\ &\quad + 2u(p)u(q) s_T(p, q) + 2u(q)u(r) s_T(q, r) \\ &\quad + 2u(r)u(p) s_T(r, p), \\ &= -s_T(p, q)(u(p) - u(q))^2 - s_T(q, r)(u(q) - u(r))^2 \\ &\quad - s_T(r, p)(u(r) - u(p))^2. \end{aligned}$$

Summing this expression over all  $T \in \mathcal{T}_h$ , and combining it with (36), we obtain (35), which concludes the proof.  $\square$



Finally, we provide an approximation of the coefficients  $\gamma_p^h$  which will be easily compared with the AD-LBR weights  $\gamma_p$  (13).

**Lemma 6.** *Consider an edge  $[p, p + he]$  of  $\mathcal{T}_h$ , shared by the two distinct triangles  $T, T' \in \mathcal{T}_h$ . Let  $hf, hg$  (resp.  $hf', hg'$ ) be the two other vector edges of  $T$  (resp.  $T'$ ), oriented so that  $e + f + g = 0$  (resp.  $e + f' + g' = 0$ ). Then, with  $M := \mathbf{M}(p)$*

$$\left| \gamma_p^h(e) + \frac{\langle f, Mg \rangle + \langle f', Mg' \rangle}{4 \det M} \right| \leq \varepsilon_h,$$

where  $\varepsilon_h := 2\nu_{\div}^2 \max\{\|\mathbf{D}(x) - \mathbf{D}(y)\|; \|x - y\| \leq 2\nu_{\div} h\}$ .

*Proof.* We assume, up to exchanging  $f$  and  $g$ , that  $[p, p - hg]$  is an edge of  $T$ . We denote  $\alpha := \det(e, f) \in \{-1, 1\}$ , see Lemma 4 (Area), and observe that  $\alpha = \det(f, g) = \deg(g, e)$ . Let  $\gamma$  be the constant value of  $\nabla\varphi_p^h$  on  $T$ . Then  $\langle \gamma, he \rangle = -1$  and  $\langle \gamma, hg \rangle = 1$ . These two independent linear identities are satisfied by  $\alpha f^\perp/h$ , which is thus equal to  $\gamma$ . We have shown that  $\nabla\varphi_p^h = \alpha f^\perp/h$  on  $T$ .

Denoting  $q := p + hg$ , we obtain likewise  $\nabla\varphi_q^h = \alpha g^\perp/h$  on  $T$ . Let  $D := \mathbf{D}(p) = M^{-1}$ , and let  $R$  be the rotation by  $\pi/2$ . Then

$$\begin{aligned} \int_T \langle \nabla\varphi_p^h, D\nabla\varphi_q^h \rangle &= \frac{h^2}{2} \left\langle \frac{\alpha f^\perp}{h}, D \frac{\alpha g^\perp}{h} \right\rangle \\ &= \frac{1}{2} \langle f, R^T D R g \rangle = \frac{1}{2} \left\langle f, \frac{M}{\det M} g \right\rangle = \frac{\langle f, Mg \rangle}{2 \det M}. \end{aligned}$$

Therefore, using Lemma 4 (Diameter) in the last step,

$$\begin{aligned} &\left| \int_T \langle \nabla\varphi_p^h, \mathbf{D}(z) \nabla\varphi_q^h \rangle dz - \frac{\langle f, Mg \rangle}{2 \det M} \right| \\ &= \left| \int_T \langle \nabla\varphi_p^h, (\mathbf{D}(z) - \mathbf{D}(p)) \nabla\varphi_q^h \rangle dz \right| \\ &\leq \frac{h^2}{2} \frac{2\nu_{\div}}{h} \frac{2\nu_{\div}}{h} \max\{\|\mathbf{D}(z) - \mathbf{D}(p)\|; z \in T\} \leq \varepsilon_h. \end{aligned}$$

Proceeding likewise on  $T'$ , and recalling (34) (or (36)), we conclude the proof.  $\square$

### 3.2 Some properties of $M$ -reduced bases

We establish some technical properties of  $M$ -reduced bases, thanks to which we will be able to compare in §3.3 the “geometric” construction of the ADT finite element stencils  $V_h$ , with “algebraic” construction of the AD-LBR stencils  $V$ .

**Lemma 7.** *Let  $M \in S_2^+$ , let  $e_1, \dots, e_n \in \mathbb{Z}^2$ ,  $n > 1$ , and let  $\varepsilon \in \{-1, 1\}$ . Assume that for all  $1 \leq i \leq n$ , with the convention  $e_{n+1} := e_1$ :*

$$\det(e_i, e_{i+1}) = \varepsilon, \quad (37)$$

$$\langle e_i, Me_{i+1} \rangle > -\frac{1}{2} \min\{\|e_i\|_M^2, \|e_{i+1}\|_M^2\}. \quad (38)$$

*Then any  $M$ -reduced basis  $(e, f)$  satisfies*

$$\{e, f\} \subset \{e_1, \dots, e_n\}.$$

*Proof.* Let  $z \in \mathbb{Z}^2 \setminus \{e_1, \dots, e_n\}$ . Our objective is to show that  $z$  cannot be the element of a  $M$ -reduced basis, and we may therefore assume that  $z$  has co-prime coordinates.

It follows from (37) that the closed polygonal line of consecutive vertices  $e_1, \dots, e_n$ , circles at least once around the origin. Hence  $z = \alpha e_i + \beta e_{i+1}$ , for some  $1 \leq i \leq n$  and some  $\alpha, \beta \geq 0$ . Since  $|\det(e_i, e_{i+1})| = 1$ ,  $\alpha$  and  $\beta$  are integers. Since  $z \notin \{e_i, e_{i+1}\}$ ,  $\alpha + \beta \geq 2$ . Since  $z$  has co-prime coordinates,  $\alpha\beta \neq 0$ .

Assuming without loss of generality that  $\|e_i\|_M \geq \|e_{i+1}\|_M$ , we obtain using (38)

$$\begin{aligned} \|z\|_M^2 &= \alpha^2 \|e_i\|_M^2 + \beta^2 \|e_{i+1}\|_M^2 + 2\alpha\beta \langle e_i, Me_{i+1} \rangle \\ &> \alpha^2 \|e_i\|_M^2 + \beta^2 \|e_{i+1}\|_M^2 - \alpha\beta \min\{\|e_i\|_M^2, \|e_{i+1}\|_M^2\} \\ &\geq \|e_i\|_M^2 + (\alpha^2 + \beta^2 - 1 - \alpha\beta) \|e_{i+1}\|_M^2. \end{aligned}$$

Observing that  $\alpha^2 + \beta^2 - 1 - \alpha\beta \geq 0$  for all  $\alpha, \beta \in [1, \infty[$ , we obtain  $\|z\|_M > \|e_i\|_M$ . Since  $e_i$  and  $e_{i+1}$  are linearly independent, we have  $\|e_i\|_M \geq \lambda_2(M)$ . Finally  $\|z\|_M > \lambda_2(M)$ , hence  $z$  cannot be the element of a  $M$ -reduced basis, which concludes the proof.  $\square$

We use in the following the shorthand

$$\begin{aligned} &\{a_1, \dots, a_n, \text{ and opposites}\} \\ &:= \{a_1, \dots, a_n\} \cup \{-a_1, \dots, -a_n\}. \end{aligned}$$

Given  $M \in S_2^+$ , and a  $M$ -reduced basis  $(e, f)$  of  $\mathbb{Z}^2$ , we denote  $\mu(M) := |\langle e, Mf \rangle|$ . This value can be expressed in terms of the Minkowski minima and thus does not depend on the particular choice of  $M$ -reduced basis. Indeed, recalling the identity

$$\langle e, Mf \rangle^2 + \det(M) \det(e, f)^2 = \|e\|_M^2 \|f\|_M^2,$$

we obtain

$$\mu(M) = |\langle e, Mf \rangle| = \sqrt{\lambda_1(M)^2 \lambda_2(M)^2 - \det(M)}. \quad (39)$$

A vanishing value,  $\mu(M) = 0$ , indicates that the lattice  $\mathbb{Z}^2$  admits an  $M$ -orthogonal basis.

We next show that the stencils of the AD-LBR do not depend on the choices of reduced bases, as was announced in the introduction.

**Lemma 8.** *The weights  $\gamma_z : \mathbb{Z}^2 \rightarrow \mathbb{R}_+$ , defined in (13) and used in the AD-LBR, do not depend on the choice of  $\mathbf{M}(z)$ -reduced basis.*

*Proof.* We denote  $M := \mathbf{M}(z)$ , and consider two  $M$ -reduced bases  $(e, f)$ ,  $(e', f')$ . We assume as in the introduction that  $\langle e, Mf \rangle \leq 0$  and  $\langle e', Mf' \rangle \leq 0$ , up to changing  $f$  or  $f'$  into its opposite. Let  $g := -e - f$  and

$g' := -e' - f'$ . Our objective is to show that the weights  $\gamma, \gamma' : \mathbb{Z}^2 \rightarrow \mathbb{R}_+$ , defined by (13) and associated to the bases  $(e, f)$ ,  $(e', f')$ , are identical.

Recall that  $\langle f, Mg \rangle$ ,  $\langle g, Me \rangle$ ,  $\langle f', Mg' \rangle$ ,  $\langle g', Me' \rangle$  are negative, see (12). Applying Lemma 7 to the family

$$(e', -g', f', -e', g', -f')$$

we obtain that

$$\{e, f\} \subset \{e', f', g', \text{and opposites}\}. \quad (40)$$

If  $\mu(M) \neq 0$ , then  $\langle e, Mf \rangle$  and  $\langle e', Mf' \rangle$  are negative, and not merely non-positive, thus  $\{e, f\} \subset \{e', f', g'\}$ , or  $\{e, f\} \subset \{-e', -f', -g'\}$ . Since  $e + f + g = 0 = e' + f' + g'$ , it follows that  $\{e, f, g\} = \{e', f', g'\}$ , or  $\{e, f, g\} = \{-e', -f', -g'\}$ . The expression (13) thus implies  $\gamma = \gamma'$ , as announced.

If  $\mu(M) = 0$ , then  $\langle e, Mf \rangle = 0 = \langle e', Mf' \rangle$ . Using again (13) we find

$$\begin{aligned} \gamma(\pm g) &= -\langle e, Mf \rangle / (2 \det M) = 0 \\ \gamma(\pm e) &= \|f\|_M^2 / (2 \det M), \\ \gamma(\pm f) &= \|e\|_M^2 / (2 \det M), \end{aligned} \quad (41)$$

and likewise for  $\gamma', e', f', g'$ . Note also that  $\|g'\|_M^2 = \|e'\|_M^2 + \|f'\|_M^2 > \lambda_2(M)^2$ , hence  $e$  and  $f$  are different from  $g'$  and  $-g'$ . It follows from (40) that  $\{e, f\} = \{\varepsilon_1 e', \varepsilon_2 f'\}$  for some  $\varepsilon_1, \varepsilon_2 \in \{-1, 1\}$ . This implies  $\gamma = \gamma'$  in view of (41), and concludes the proof.  $\square$

We saw in the introduction (11) that

$$2\mu(M) \leq \lambda_1(M)^2. \quad (42)$$

The next lemma establishes weak unicity and stability properties for  $M$ -reduced bases, when the inequality (42) is not saturated.

**Lemma 9.** *Consider  $M, M' \in S_2^+$ , a  $M$ -reduced basis  $(e, f)$ , and a  $M'$ -reduced basis  $(e', f')$ . Let  $\tau \geq 1$  be such that  $\tau^{-2}M \leq M' \leq \tau^2 M$ , in the sense of symmetric matrices. Assume either:*

- $2\mu(M) < \lambda_1(M)^2$ , and  $\tau = 1$  (i.e.  $M' = M$ ).
- $4\mu(M) \leq \lambda_1(M)^2$ , and  $\tau^4 \leq 1 + \frac{1}{3}\kappa(M)^{-2}$ .

Then  $\{e', f'\} \subset \{e, f, \text{and opposites}\}$ .

*Proof.* Denoting  $\alpha := 2\mu(M)/\lambda_1(M)^2$ , we obtain:

$$\begin{aligned} 4\langle e, M'f \rangle &= \|e + f\|_{M'}^2 - \|e - f\|_{M'}^2 \\ &\leq \tau^2 \|e + f\|_M^2 - \tau^{-2} \|e - f\|_M^2 \\ &= (\tau^2 - \tau^{-2})(\|e\|_M^2 + \|f\|_M^2) + 2(\tau^2 + \tau^{-2})\langle e, Mf \rangle \\ &\leq ((\tau^2 - \tau^{-2})(1 + \kappa(M)^2) + \alpha(\tau^2 + \tau^{-2}))\|e\|_M^2 \\ &\leq ((\tau^4 - 1)(1 + \kappa(M)^2) + \alpha(\tau^4 + 1))\|e\|_{M'}^2. \end{aligned}$$

We used  $\|f\|_M \leq \kappa(M)\|e\|_M$ , see (24), in the fourth line. Replacing  $\alpha$  and  $\tau$  with their assumed upper bounds, we obtain  $2\langle e, M'f \rangle < \|e\|_{M'}^2$ . Proceeding likewise, we obtain  $2|\langle e, M'f \rangle| < \min\{\|e\|_{M'}^2, \|f\|_{M'}^2\}$ . We may therefore apply Lemma 7 to  $M'$  and  $(e, f, -e, -f)$ , and obtain  $\{e', f'\} \subset \{e, f, -e, -f\}$  as announced.  $\square$

### 3.3 Comparison of the stencils

We assume in this subsection that the scale parameter  $h$  is sufficiently small. Our assumption is stronger than the one used in §3.1, see (30), hence in particular there exists an Anisotropic Delaunay Triangulation  $\mathcal{T}_h$ . More precisely we assume that

$$\tau_h \leq \sqrt[4]{1 + \frac{1}{3}\nu_{\dot{\cdot}}^{-2}} \quad \text{and} \quad \theta_h \leq \theta_0 := \frac{\nu_1^2}{4}. \quad (43)$$

See (26), (29), and Lemma 4 for the definition  $(\nu_1, \nu_{\dot{\cdot}})$ ,  $\tau_h$  and  $\theta_h$  respectively. For Lipschitz metrics,  $\tau_h = 1 + \mathcal{O}(h)$  and  $\theta_h = \mathcal{O}(h)$ .

Our objective is to compare the stencils  $V(p)$ ,  $V_h(p)$ , of the AD-LBR (14) and of the ADT finite element discretization (19) respectively, at a point  $p \in h\mathbb{Z}^2$ . The next lemma shows that they are equal *unless* the lattice  $\mathbb{Z}^2$  is almost orthogonal with respect to the local metric; a property quantified via  $\mu(\mathbf{M}(p))$ , see (39).

**Lemma 10.** *Let  $p \in h\mathbb{Z}^2$ , and let  $M := \mathbf{M}(p)$ . If  $\mu(M) > \theta_h$ , then  $V_h(p) = V(p)$ . In any case, one has for any  $M$ -reduced basis  $(e, f)$ :*

$$V_h(p) \supset \{e, f, \text{and opposites}\} \quad (44)$$

$$V_h(p) \subset \{e, f, e + f, e - f, \text{and opposites}\}. \quad (45)$$

*Proof.* We assume that  $\langle e, Mf \rangle \leq 0$ , up to replacing  $f$  with  $-f$ . Let  $T \in \mathcal{T}_h$  be a triangle containing  $p$ , and let  $he_1, he_2, he_3$  be the edges of  $T$ , oriented so that  $e_1 + e_2 + e_3 = 0$ . Using Lemma 4 (Acuteness), we obtain for all  $1 \leq i \leq 3$ , with the convention  $e_4 := e_1$

$$\langle e_i, Me_{i+1} \rangle \leq \theta_h \leq \theta_0 < \frac{1}{2}\nu_1^2 \leq \frac{1}{2} \min\{\|e_i\|_M^2, \|e_{i+1}\|_M^2\}.$$

Denote  $E := \{e_1, e_2, e_3\}$ , and  $-E := \{-e_1, -e_2, -e_3\}$ . Applying Lemma 7 to  $M$  and the points  $(e_1, -e_3, e_2, -e_1, e_3, -e_2)$ , we obtain that  $\{e, f\} \subset E \cup (-E)$ . Up to exchanging  $E$  with  $-E$ , we thus have  $\{e, f\} \subset E$  or  $\{e, -f\} \subset E$ . Since the elements of  $E$  sum to zero, we conclude that

$$E = \{e, f, -e - f\} \quad \text{or} \quad E = \{e, -f, -e + f\}, \quad (46)$$

which implies (45).

If  $\mu(M) = |\langle e, Mf \rangle| > \theta_h$ , then Lemma 4 (Acuteness) forbids the second case in (46). Thus  $E = \{e, f, -e - f\}$ , and therefore  $V_h(p) \subset V(p)$ .

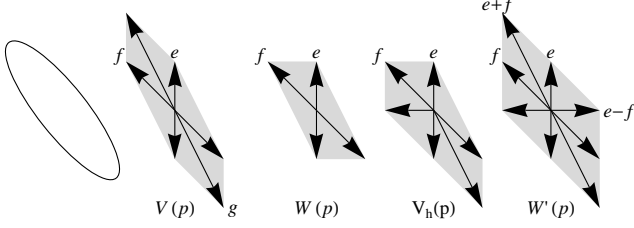


Figure 4: Consider a point  $p \in h\mathbb{Z}^2$ , and denote  $M := \mathbf{M}(p)$ . From left to right: ellipse  $\{\|z\|_M \leq 1\}$ , AD-LBR stencil  $V(p)$ , stencils  $W(p) \subset V_h(p) \subset W'(p)$ . For  $W(p)$  and  $W'(p)$  we assumed that  $\mu(M) < \theta_0$ , otherwise they are equal to  $V(p)$ . Note that  $V(p)$ ,  $W(p)$ ,  $W'(p)$  only depend on  $M$ , while  $V_h(p)$  depends on the structure of the triangulation  $\mathcal{T}_h$ .

Let  $T \in \mathcal{T}_h$  be a triangle containing  $p$  and intersecting the half line  $L := \{p + re; r > 0\}$ . We know (46) that  $e$  is a vector edge of  $T$ . The corresponding edge segment must be  $[p, p + he]$ , since otherwise  $T \cap L$  would be empty. Thus  $e \in V_h(p)$ . Applying the same argument to  $-e, f, -f$ , we obtain (44).

If  $\mu(M) > \theta_h$ , then  $e + f$  is also a vector edge of any triangle  $T \in \mathcal{T}_h$  containing  $p$ , since we eliminated the second case in (46). Reasoning as above we find that  $\{e + f, -e - f\} \subset V_h(p)$ , and therefore  $V(p) \subset V_h(p)$ . Thus  $V(p) = V_h(p)$ . This concludes the proof.  $\square$

We introduce new stencils  $W(p), W'(p)$ , where  $p \in \mathbb{R}^2$ ,  $M := \mathbf{M}(p)$ , defined as follows. If  $\mu(M) \leq \theta_0$ , then denoting by  $(e, f)$  a  $M$ -reduced basis,

$$W(p) := \{e, f, \text{and opposites}\}, \quad (47)$$

$$W'(p) := \{e, f, e + f, e - f, \text{and opposites}\}. \quad (48)$$

On the other hand, if  $\mu(M) > \theta_0$ , then

$$W(p) := V(p) =: W'(p). \quad (49)$$

Note that  $W(p) \subset V_h(p) \subset W'(p)$ , for any  $p \in h\mathbb{Z}^2$ , since  $\theta_h \leq \theta_0$  by assumption (43).

**Lemma 11.** *The stencils  $W(p), W'(p)$ , do not depend on the choice of  $\mathbf{M}(p)$ -reduced basis.*

*Proof.* Let  $M := \mathbf{M}(p)$ . If  $\mu(M) > \theta_0$ , then  $W(p), W'(p)$  are defined by (49), hence here is nothing to prove. Otherwise we obtain  $\mu(M) \leq \theta_0 \leq \nu_1^2/4 \leq \lambda_1(M)^2/4$ . Hence, by Lemma 9, any two  $M$ -reduced bases  $(e, f), (e', f')$ , need to satisfy  $\{e', f'\} \subset \{e, f, \text{and opposites}\}$ . In view of (47) and (48), they thus yield the same stencils  $W(p), W'(p)$ .  $\square$

Let  $\mathcal{F}_h, \mathcal{F}'_h$  be the energies associated to the stencils

$W, W'$ : for  $u \in L^2(\Omega_h)$ , extended to  $h\mathbb{Z}^2$  by periodicity,

$$\mathcal{F}_h(u) := \sum_{z \in \Omega_h} \sum_{g \in W(z)} |u(z + hg) - u(z)|^2,$$

$$\mathcal{F}'_h(u) := \sum_{z \in \Omega_h} \sum_{g \in W'(z)} |u(z + hg) - u(z)|^2.$$

The outline of the proof of theorem 1 is as follows. We prove in Lemmas 13, 14 and 12 respectively that for any  $u \in L^2(\Omega_h)$ :

$$|\mathcal{E}'_h(u) - \mathcal{E}_h(u)| \leq C_0(\theta_h + \varepsilon_h)\mathcal{F}'_h(u) \quad (50)$$

$$\mathcal{F}'_h(u) \leq C_1\mathcal{F}_h(u) \quad (51)$$

$$\mathcal{F}_h(u) \leq C_2\mathcal{E}_h(u), \quad (52)$$

where the constants  $C_0, C_1, C_2$  only depend on the metric  $\mathbf{M}$ . Combining these inequalities, and recalling that  $\theta_h = \mathcal{O}(h)$  and  $\varepsilon_h = \mathcal{O}(h)$  for Lipschitz metrics ( $\varepsilon_h$  is defined in Lemma 6), we obtain

$$|\mathcal{E}'_h(u) - \mathcal{E}_h(u)| \leq ch\mathcal{E}_h(u),$$

for some constant  $c = c(\mathbf{M})$ . This establishes (16), and concludes the proof of Theorem 1.

For each  $p \in \mathbb{R}^2$ , we denote by  $\eta_p, \eta'_p : \mathbb{Z}^2 \rightarrow \{0, 1\}$ , the characteristic functions of  $W(p)$  and  $W'(p)$  respectively. The proofs of (50) and (52) immediately result from the comparison, in Lemmas 13 and 12 respectively, of the coefficients  $\gamma_p, \gamma_p^h, \eta_p, \eta'_p$  appearing in the expressions of  $\mathcal{E}_h, \mathcal{E}'_h, \mathcal{F}_h, \mathcal{F}'_h$ .

**Lemma 12.** *For any  $p \in \mathbb{R}^2$ , one has on  $\mathbb{Z}^2$*

$$\eta_p \leq C_2\gamma_p, \quad \text{with } C_2 := 2\theta_0^{-1} \max\{\det \mathbf{M}(q); q \in \Omega\}.$$

*Proof.* Let  $M := \mathbf{M}(p)$ , and let  $(e, f)$  be a  $M$ -reduced basis. It follows from (12) that

$$2 \det(M)\gamma_p(\pm f) \geq \frac{1}{2}\|e\|_M^2 \geq \frac{1}{2}\nu_1^2 = 2\theta_0,$$

and likewise for  $\gamma_p(\pm e)$ . If  $\mu(M) \leq \theta_0$ , then  $W(p) = \{e, f, \text{and opposites}\}$ , and this concludes the proof.

Assume now that  $\mu(M) > \theta_0$ . Assume also that  $\langle e, Mf \rangle \leq 0$ , and denote  $g := -e - f$ . We have  $W(p) = \{e, f, g, \text{and opposites}\}$ , and we obtain as announced

$$2 \det(M)\gamma_p(\pm g) = -\langle e, Mf \rangle = \mu(M) \geq \theta_0. \quad \square$$

Let  $p \in h\mathbb{Z}^2$  and let  $e_1, \dots, e_k$  be the consecutive elements of  $V_h(p)$ , in trigonometric order. We define for all  $1 \leq i \leq k$ , denoting  $M := \mathbf{M}(p)$ ,

$$\tilde{\gamma}_p^h(e_i) := -\frac{\langle e_i - e_{i-1}, Me_{i-1} \rangle + \langle e_i - e_{i+1}, Me_{i+1} \rangle}{4 \det M},$$

with the periodic conventions  $e_{k+1} := e_1, e_0 := e_k$ . We also set  $\tilde{\gamma}_p^h = 0$  on  $\mathbb{Z}^2 \setminus \{e_1, \dots, e_k\}$ .

**Lemma 13.** For any  $p \in h\mathbb{Z}^2$ , one has on  $\mathbb{Z}^2$

$$|\gamma_p^h - \tilde{\gamma}_p^h| \leq \varepsilon_h \eta_p', \quad \text{and} \quad |\tilde{\gamma}_p^h - \gamma_p| \leq C_0 \theta_h \eta_p', \quad (53)$$

where  $\varepsilon_h$  is given in Lemma 6, and  $C_0^{-1} := \min\{\det \mathbf{M}(q); q \in \Omega\}$ .

*Proof.* The coefficients  $\gamma_p, \gamma_p^h, \tilde{\gamma}_p^h$ , are all equal to zero outside of  $W'(p)$ . This holds by construction of  $\gamma_p$ , and by Lemma 10 for  $\gamma_p^h, \tilde{\gamma}_p^h$ . We may therefore forget about the presence of  $\eta_p'$  in (53).

First inequality. Lemma 6 states that  $|\gamma_p^h - \tilde{\gamma}_p^h| \leq \varepsilon_h$  on  $\mathbb{Z}^2$ , which concludes the proof.

Second inequality. If  $\mu(M) > \theta_h$ , then  $V_h(p) = V(p)$ . Comparing the definition of  $\tilde{\gamma}_p^h$  with that of  $\gamma_p$  (13) we observe that  $\tilde{\gamma}_p^h = \gamma_p$  on  $\mathbb{Z}^2$ , which concludes the proof in this case.

Assume now that  $\mu(M) \leq \theta_h$ , and denote by  $(e, f)$  a  $M$ -reduced basis. Looking at (12) and denoting  $\delta := 2 \det(M)$ , we find that

$$|\delta \gamma_p(\pm e) - \|f\|_M^2| = |\langle e, Mf \rangle| = \mu(M) \leq \theta_h.$$

Likewise  $|\delta \gamma_p(\pm f) - \|e\|_M^2| \leq \theta_h$ . Assuming that  $\langle e, Mf \rangle \leq 0$ , we obtain in addition

$$\delta \gamma_p(\pm(e+f)) = \mu(M) \leq \theta_h, \quad \text{and} \quad \gamma_p(\pm(e-f)) = 0.$$

Combining the definition of  $\tilde{\gamma}_p^h$  with the description of the stencil  $V_h(p)$  in Lemma 10, we obtain that

$$2\delta \tilde{\gamma}_p^h(e) = \left\{ \begin{array}{c} \langle f - e, Mf \rangle \\ \text{or} \\ \langle f + e, Mf \rangle \end{array} \right\} + \left\{ \begin{array}{c} \langle f - e, Mf \rangle \\ \text{or} \\ \langle f + e, Mf \rangle \end{array} \right\}.$$

In any case  $|\delta \tilde{\gamma}_p^h(e) - \|f\|_M^2| \leq \theta_h$ . The expressions and estimates of  $\tilde{\gamma}_p^h$  at the points  $-e, f, -f$  are obtained similarly. Likewise, using Lemma 10,

$$2\delta \tilde{\gamma}_p^h(e+f) = \begin{cases} \langle e, Mf \rangle + \langle e, Mf \rangle & \text{if } e+f \in V_h(p), \\ 0 & \text{otherwise.} \end{cases}$$

In any case  $|\delta \tilde{\gamma}_p^h(e+f)| \leq \theta_h$ . The expressions and estimates of  $\tilde{\gamma}_p^h$  at the points  $-(e+f), e-f, -(e-f)$  are similar. Comparing the above estimates of  $\gamma_p, \tilde{\gamma}_p^h$ , we obtain that  $\delta|\gamma_p - \tilde{\gamma}_p^h| \leq 2\theta_h$  on  $\{e, f, e+f, e-f, \text{and opposites}\} = W'(p)$ . Observing that  $\delta = 2 \det(M) \geq 2C_0^{-1}$ , we conclude the proof.  $\square$

In the next and last lemma, we control the contribution to the energy  $\mathcal{F}'_h$  of a stencil  $W'(p)$ ,  $p \in h\mathbb{Z}^2$ , in terms of the contributions to  $\mathcal{F}_h$  of  $W(p)$  and of the neighboring stencils  $W(p+he)$ ,  $e \in W(p)$ . This leads to an estimate of  $\mathcal{F}'_h$  in terms of  $\mathcal{F}_h$ , which concludes the proof of Theorem 1.

**Lemma 14.**  $\mathcal{F}'_h(u) \leq C_1 \mathcal{F}_h(u)$ , for any  $u \in L^2(\Omega_h)$ , with  $C_1 := 17$ .

*Proof.* Consider a grid point  $p \in h\mathbb{Z}^2$ , and denote  $M := \mathbf{M}(p)$ . Assume first that  $\mu(M) \leq \theta_0$ , so that  $W(p) \subsetneq W'(p)$ . Consider also an arbitrary  $g \in W'(p) \setminus W(p)$ , and observe that  $g = e + f$  for some  $M$ -reduced basis  $(e, f)$ .

We set  $p' := p + e$  and  $M' := \mathbf{M}(p')$ . Applying the second point of Lemma 9, we find that  $(e, f)$  is also a  $M'$ -reduced basis. Indeed we have as required

$$4\mu(M) \leq 4\theta_0 = \nu_1^2 \leq \|M^{-1}\|^{-1} \leq \lambda_1(M)^2,$$

and the assumption on  $\tau$  follows from (43) and (28). Therefore

$$f \in W(p'), \quad \text{and} \quad h^{-1}(p' - p) = e \in W(p'). \quad (54)$$

We obtain

$$\begin{aligned} & |u(p+g) - u(p)|^2 \\ &= |u(p+e+f) - u(p)|^2 \\ &\leq 2(|u(p+e+f) - u(p+e)|^2 + |u(p+e) - u(p)|^2) \\ &= 2(|u(p'+f) - u(p')|^2 + |u(p+e) - u(p)|^2). \end{aligned} \quad (55)$$

Denote, for all  $q \in h\mathbb{Z}^2$ ,

$$\begin{aligned} \mathcal{F}_h(u; q) &:= \sum_{g \in W(q)} |u(q+hg) - u(q)|^2, \\ \mathcal{F}'_h(u; q) &:= \sum_{g \in W'(q)} |u(q+hg) - u(q)|^2. \end{aligned}$$

Using (55), we obtain

$$\mathcal{F}'_h(u; p) - \mathcal{F}_h(u; p) \leq \mathcal{G}_h(u; p) \quad (56)$$

where  $\mathcal{G}_h(u; p)$  is given by

$$\begin{cases} 4\mathcal{F}_h(u; p) + 2 \sum_{g \in W(p)} \mathcal{F}_h(u; p+g), & \text{if } \mu(\mathbf{M}(p)) \leq \theta_0 \\ 0 & \text{if } \mu(\mathbf{M}(p)) > \theta_0 \end{cases}$$

When  $\mathcal{F}_h(u; p')$  appears in  $\mathcal{G}_h(u; p)$ , with  $p, p' \in h\mathbb{Z}^2$ ,  $p \neq p'$ , we have  $h^{-1}(p' - p) \in W(p')$ , see (54). For each  $p' \in h\mathbb{Z}^2$ , there are thus at most  $\#(W(p')) \leq 6$  points  $p \in h\mathbb{Z}^2 \setminus \{p'\}$  such that  $\mathcal{F}_h(u; p')$  appears in  $\mathcal{G}_h(u; p)$ . Summing (56) over  $p \in \Omega_h$ , we thus obtain  $\mathcal{F}'_h(u) - \mathcal{F}_h(u) \leq (4+2 \times 6)\mathcal{F}_h(u)$  (the constant could easily be improved), which concludes the proof.  $\square$

## 4 Numerical experiments

We compare our scheme AD-LBR with a family of other schemes: finite difference, finite elements, and two schemes from the image processing literature. We begin with a quantitative comparison for the discretization of the restoration equation, in a synthetic case where the exact solution is analytically available for reference. The second test case is a qualitative comparison of Coherence-Enhancing Diffusion (CED), on a real image and the quality assessment is by visual inspection. Finally we present a 3D implementation of CED, based on AD-LBR, for proof of feasibility.

## 4.1 The different schemes

- AD-LBR: the scheme presented in this work.
- Finite Differences (FD). The gradient and the divergence are discretized using finite differences, the matrix  $\mathbf{D}$  is discretized at the cells. More precisely the gradient is discretized by

$$\begin{aligned}(\partial_x u)_{i+1/2,j} &= u_{i+1,j} - u_{i,j} \\ (\partial_y u)_{i,j+1/2} &= u_{i,j+1} - u_{i,j},\end{aligned}$$

and the divergence is defined as follows:

$$\begin{aligned}\operatorname{div}(\mathbf{D}\nabla u)_{i,j} &= \partial_x(\mathbf{D}^{11}\partial_x u + \mathbf{D}^{12}\partial_y u)_{i,j} \\ &\quad + \partial_y(\mathbf{D}^{21}\partial_x u + \mathbf{D}^{22}\partial_y u)_{i,j},\end{aligned}$$

with

$$\begin{aligned}(\mathbf{D}^{11}\partial_x u)_{i+1/2,j} &= \frac{1}{2} \left( \mathbf{D}_{i+1/2,j+1/2}^{11} + \mathbf{D}_{i+1/2,j-1/2}^{11} \right) (\partial_x u)_{i+1/2,j}, \\ \partial_x(\mathbf{D}^{11}\partial_x u)_{i,j} &= (\mathbf{D}^{11}\partial_x u)_{i+1/2,j} - (\mathbf{D}^{11}\partial_x u)_{i-1/2,j} \\ (\mathbf{D}^{21}\partial_x u)_{i+1/2,j+1/2} &= \mathbf{D}_{i+1/2,j+1/2}^{21} \frac{1}{2} \left( (\partial_x u)_{i+1/2,j} + (\partial_x u)_{i+1/2,j+1} \right), \\ \partial_y(\mathbf{D}^{21}\partial_x u)_{i,j} &= \frac{1}{2} \left( (\mathbf{D}^{21}\partial_x u)_{i+1/2,j+1/2} - (\mathbf{D}^{21}\partial_x u)_{i+1/2,j-1/2} \right. \\ &\quad \left. + (\mathbf{D}^{21}\partial_x u)_{i-1/2,j+1/2} - (\mathbf{D}^{21}\partial_x u)_{i-1/2,j-1/2} \right),\end{aligned}$$

and similar terms involve  $\partial_y u$ . This amounts to discretize the term  $\operatorname{div}(\mathbf{D}\nabla u)$  using a stencil of 9 points, where the coefficients depend on the matrix  $\mathbf{D}$ .

- Bilinear Finite Elements (Q1). Bilinear finite elements, also referred to as Q1 finite elements, are linear with respect to each space direction. This amounts to use a 9 points stencil, where the coefficients are different from the previous scheme.
- Scharf-Weickert scheme (SW). This scheme, introduced in [16], is based on a second order approximation of the gradient using a  $3 \times 3$  centered stencil. As a result, it offers good accuracy and rotation invariance when applied to a sufficiently smooth function, but lacks robustness guarantees such as the discrete maximum principle and spectral correctness (see §1), even for  $\mathbf{D} = \operatorname{Id}$ . The stencil for this scheme has size  $5 \times 5$ .
- Weickert's Non-Negative scheme (W-NN). The coefficients of this scheme, detailed in [14] page 95, are non-negative as long as the anisotropy satisfies  $\kappa \leq 1 + \sqrt{2} \sim 2.41$ .

To fix the ideas and illustrate the difference between the schemes, we propose to compute the stencil and the coefficients for different *constant* diffusion tensors  $\mathbf{D}$ , in isotropic and anisotropic cases. Denoting by  $R$  the matrix of rotation by the angle  $\theta = \pi/6$ , and by  $\kappa \geq 1$  the chosen anisotropy ratio, we set, identically on  $\mathbb{R}^2$ :

$$\mathbf{D} := R \begin{pmatrix} 1 & 0 \\ 0 & \kappa^{-2} \end{pmatrix} R^T. \quad (57)$$

The results are presented in Tables 1 and 2. Note that for the two last cases (anisotropy  $\kappa = \sqrt{10}$  and  $\kappa = \sqrt{50}$ ) the AD-LBR stencil contains points that are further than the  $3 \times 3$  neighborhood of the pixel. However the stencil contains 6 points, as expected. This contrasts with the schemes FD, Q1, W-NN where only the  $3 \times 3$  neighborhood is involved. Another observation is that the off-center stencil coefficients of the AD-LBR are non-positive (this gives non-positive off-diagonal coefficients for  $-\operatorname{div}(\mathbf{D}\nabla)$ ), in contrast with schemes FD, Q1, SW, and with scheme W-NN for anisotropy  $\kappa > 1 + \sqrt{2}$ . This is an essential property of AD-LBR, see (5), and as a consequence our scheme satisfies, unconditionally, the discrete maximum principle [1, 3].

The largest eigenvalue of the discrete operator  $-\operatorname{div}(\mathbf{D}\nabla)$  is given in Table 3, for the different schemes. It turns out that AD-LBR has in most cases the smallest eigenvalues among all schemes, excepted scheme SW. This property allows (although this was not done in our numerical experiments) to use larger time steps for AD-LBR than for the other schemes, when solving parabolic equations (2) or (60) with an explicit time discretization.

**Remark 2** (Additive Operator Splitting). *Denote by  $A$  the symmetric  $N \times N$  non-negative matrix associated to the AD-LBR energy  $\mathcal{E}_h$  (3), where  $N := \#(\Omega_h)$ . Let also  $U \in \mathbb{R}^N$  be the vector of values of  $u \in L^2(\Omega_h)$ , so that  $U^T A U = \mathcal{E}_h(u)$ . The explicit numerical scheme (used in §4.4 and §4.5) for the parabolic PDE (2) has the form  $U' = (1 - \tau A)U$ , where the time step should satisfy  $0 < \tau \leq 2/\|A\|$  for stability. Additive Operator Splitting (AOS) [15] allows larger time steps, by introducing a semi implicit scheme*

$$U' = \frac{1}{m} \sum_{1 \leq i \leq m} (1 + m\tau A_i)^{-1} (1 - \tau \tilde{A})U,$$

where  $A = A_0 + \dots + A_m + \tilde{A}$ . For this to be useful, the matrices  $1 + m\tau A_i$  should be easy to invert. The matrix  $\tilde{A}$  should be symmetric, non-negative, and its norm  $\|\tilde{A}\|$  should be significantly smaller than  $\|A\|$ , so that larger time steps  $0 < \tau \leq 2/\|\tilde{A}\|$  can be used.

The AD-LBR is completely compatible with this approach, since the discrete energy (3) can be written as the

sum of the simpler energies:

$$\mathcal{E}_h^e(u) = h^{d-2} \sum_{z \in \Omega_j} \gamma(z, e) (|u(z + he) - u(z)|^2 + |u(z - he) - u(z)|^2),$$

where  $e$  ranges over elements of  $\mathbb{Z}^2$  greater than  $(0, 0)$  in lexicographic order, and with co-prime coordinates. The  $N \times N$  symmetric non-negative matrix  $A_e$ , representing the energy  $\mathcal{E}_h^e$ , is tridiagonal if  $\Omega_h$  is enumerated in lines directed by  $e$ ; hence the inversion of  $1 + m\tau A_e$  has cost  $\mathcal{O}(N)$ . AOS could be applied to the decomposition  $A = A_{e_1} + \dots + A_{e_s} + \tilde{A}$ , with suitably chosen  $e_1, \dots, e_s$ , e.g.  $(1, 0)$ ,  $(0, 1)$ ,  $(1, 1)$ ,  $(1, -1)$ . This acceleration procedure was not used in our numerical experiments.

Table 1: The stencil coefficients for different constant diffusion tensors, and the different schemes presented. The value of the anisotropy  $\kappa$  is given in the second row, and the orientation of the principal axis is  $\theta = \pi/6$ , see (57). The bold coefficient indicates the center node. In some examples we present for clarity reasons only half of the stencil (the other half can be deduced by symmetry). Stencil entries are highlighted when they are positive and off-center - an undesirable property which gives rise to stability issues.

$\kappa$	$\kappa = 1$ ( $\mathbf{D} = \text{Id}$ )	$\kappa = \sqrt{2}$
stencil for AD-LBR	0 -1 0 -1 <b>4</b> -1 0 -1 0	0 -0.41 -0.22 -0.66 <b>2.57</b> -0.66 -0.22 -0.41 0
stencil for FD	0 -1 0 -1 <b>4</b> -1 0 -1 0	<b>0.11</b> -0.63 -0.11 -0.88 <b>3</b> -0.88 -0.11 -0.63 <b>0.11</b>
stencil for Q1	$\frac{1}{3} \begin{pmatrix} -1 & -1 & -1 \\ -1 & \mathbf{8} & -1 \\ -1 & -1 & -1 \end{pmatrix}$	-0.14 -0.13 -0.36 -0.38 <b>2</b> -0.38 -0.36 -0.13 -0.14
stencil for SW	-0.1 -0.06 -0.02 <b>0.12</b> 0 -0.06 <b>0.46</b> <b>0.12</b> -0.1 <b>0.12</b> 0 -0.06 -0.1 -0.06 -0.02	-0.06 -0.05 -0.02 <b>0.01</b> -0.04 -0.06 <b>0.35</b> <b>0.07</b> -0.09 <b>0.01</b> <b>0.04</b> -0.04 -0.06 -0.02 -0.01
stencil for W-NN	0 -1 0 -1 <b>4</b> -1 0 -1 0	0 -0.41 -0.22 -0.66 <b>2.57</b> -0.66 -0.22 -0.41 0

## 4.2 A test case with an explicit solution

Consider an image  $v \in L^2(\Omega)$ , defined on a domain  $\Omega$ , and a diffusion tensor field  $\mathbf{D} : \Omega \rightarrow S_2^+$ . A classical approach to restore the image  $v$ , if it has been corrupted by additive noise, is to find  $u \in H^1(\Omega)$  which minimizes:

$$j(u) = \int_{\Omega} |u - v|^2 + \lambda \int_{\Omega} \|\nabla u\|_{\mathbf{D}}^2. \quad (58)$$

Table 2: The stencil coefficients for different metrics and the different schemes presented, similarly to Table 1 but with more pronounced anisotropies.

$\kappa$	$\kappa = \sqrt{10}$			$\kappa = \sqrt{50}$		
stencil for AD-LBR	0 -0.26 -0.06 <b>1.16</b> -0.26 0	0 -0.11 -0.16 <b>0.55</b> -0.01 0				
stencil for FD	<b>0.19</b> -0.32 -0.19 -0.77 <b>2.2</b> -0.77 -0.19 -0.32 <b>0.19</b>	<b>0.21</b> -0.27 -0.21 -0.76 <b>2.04</b> -0.76 -0.21 -0.27 <b>0.21</b>				
stencil for Q1	<b>0.01</b> <b>0.04</b> -0.38 -0.41 <b>1.47</b> -0.41 -0.38 <b>0.04</b> <b>0.01</b>	<b>0.04</b> <b>0.08</b> -0.38 -0.42 <b>1.36</b> -0.42 -0.38 <b>0.08</b> <b>0.04</b>				
stencil for SW	-0.02 -0.04 -0.02 <b>0.09</b> -0.08 -0.07 <b>0.25</b> <b>0.04</b> -0.08 <b>0.09</b> <b>0.08</b> -0.02 -0.02 <b>0.004</b> -0.003	-0.02 -0.04 -0.02 <b>0.09</b> -0.08 -0.07 <b>0.24</b> <b>0.03</b> -0.08 <b>0.09</b> <b>0.08</b> -0.02 -0.02 <b>0.01</b> -0.002				
stencil for W-NN	0 <b>0.06</b> -0.39 -0.39 <b>1.42</b> -0.39 -0.39 <b>0.06</b> 0	0 <b>0.16</b> -0.42 -0.33 <b>1.19</b> -0.33 -0.42 <b>0.16</b> 0				

Table 3: Largest eigenvalue of the discretized operator  $-\text{div}(\mathbf{D}\nabla)$ , for the constant metric  $\mathbf{D} = D$ , where the matrix  $D$  is given on Tables 1 and 2. The time step, in the explicit discretization of (60), should not exceed the inverse of this value, see Remark 2.

$\kappa$	$\kappa = 1$	$\kappa = \sqrt{2}$	$\kappa = \sqrt{10}$	$\kappa = \sqrt{50}$
eigenvalue AD-LBR	8	4.27	2.06	1.06
eigenvalue FD	8	6.22	5.06	4.85
eigenvalue Q1	5.7	4.94	4.32	4.20
eigenvalue SW	1	1	1	1
eigenvalue W-NN	8	4.27	3.1	3.02

In other words,  $u$  is a penalized least squares approximation of  $v$ . The parameter  $\lambda > 0$  should be adjusted so as to avoid excessive smoothing (for large  $\lambda$ ), or insufficient denoising (for small  $\lambda$ ). The solution  $u$  can be characterized as the solution to the static elliptic PDE:

$$\begin{cases} -\lambda \text{div}(\mathbf{D}\nabla u) + u = v, & \text{on } \Omega. \\ \nabla u \cdot n = 0, & \text{on } \partial\Omega. \end{cases} \quad (59)$$

In applications [11, 13] the diffusion tensor  $\mathbf{D}$  is usually adapted to the local image structure, in order to avoid smoothing the edges of  $v$ . We construct below a test case (image  $v$  and tensor field  $\mathbf{D}$ ), for which the solution  $u$  is known analytically.

In order to obtain an analytic solution, we first consider a separable problem where the image is invariant by translation along the horizontal axis, and the metric is constant with axes parallel to the coordinate axes. This first prob-

lem is invariant under translations along the  $x$ -axis, and therefore boils down to a 1-dimensional problem. This separable problem is then transported by a diffeomorphism in order to obtain a new problem where the axes of the metric are no more parallel to the coordinate axes.

The analytical image is composed of a black and a white stripe:  $v_0(x) = \mathbf{1}_{x_1 > 0.5}$ , where  $x = (x_1, x_2)$ , see Figure 5. Given  $\kappa \geq 1$ , we consider the constant diffusion tensor

$$\mathbf{D}_0 = \begin{pmatrix} \kappa^{-2} & 0 \\ 0 & 1 \end{pmatrix}.$$

The analytical solution  $u_0$  of (59), applied to  $\mathbf{D}_0$ ,  $v_0$ , is known in the case of the infinite domain  $\Omega = \mathbb{R}^2$ . In Fourier domain all the coefficients are real and:

$$\widehat{u}_0(\xi) = \widehat{v}_0(\xi)/(1 + \langle \xi, \mathbf{D}_0 \xi \rangle).$$

This separable problem is transformed using the following diffeomorphism: for  $x = (x_1, x_2) \in \Omega$

$$f(x_1, x_2) = (x_1, x_2 + \alpha \cos(2\pi x_1)).$$

The jacobian of  $f$  is

$$J(x_1, x_2) = \begin{pmatrix} 1 & 0 \\ -2\alpha \sin(2\pi x_1) & 1 \end{pmatrix}$$

We apply the different restoration schemes to the image  $v = v_0 \circ f$ , and the following diffusion tensor:

$$\begin{aligned} \mathbf{D}(x) &= |\det J(x)| \cdot J(x)^{-1} \mathbf{D}_0 J(x)^{T^{-1}} \\ &= J(x)^{-1} \mathbf{D}_0 J(x)^{T^{-1}} = c \begin{pmatrix} 1 & s \\ s & s^2 + 1/\kappa^2 \end{pmatrix}, \end{aligned}$$

where we denoted  $s = 2\pi\alpha \sin(2\pi x_1)$ . The numerical solution is compared to the analytical function  $u = u_0 \circ f$ , which is the exact solution in the case of the infinite domain  $\Omega = \mathbb{R}^2$ . This numerical solution was obtained on the bounded domain  $\Omega = [0, 1]^2$ , equipped with reflecting boundary conditions. Numerical evidence suggests that this change of domain and of boundary conditions has only an anecdotic impact on the solution of (59), with the parameters chosen in this test case.

We used  $\alpha := 1/3$  in the numerical experiments. The maximum value of  $\kappa(\mathbf{D}(x))$ , among all  $x \in \Omega$ , is equivalent to  $\kappa_{\max} := \sqrt{1 + (2\pi\alpha)^2} \kappa \simeq 2.3\kappa$ .

### 4.3 Results for the synthetic test case

We present in Figure 6 the performance results of the different schemes, for different values of the anisotropy  $\kappa$ , obtained on a series of grids of size ranging from  $50 \times 50$  to  $1200 \times 1200$ . The anisotropy varies from  $\kappa = 2$  to  $\kappa = 10$ , which are relevant values for imaging applications, see the numerical experiments in §4.4. The quality of a scheme

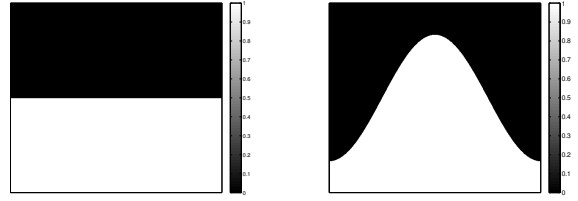


Figure 5: Left: image  $v_{\text{ana}}$ . Right: image  $v = v_{\text{ana}} \circ f$  transformed by the diffeomorphism  $f$ .

is measured by the  $L^2$  difference and the  $H^1$  semi-norm difference between the numerical solution and the analytical solution. Note that the error is concentrated close to the discontinuity, since the solution tends rapidly to a constant (0 or 1) far from the discontinuity. We chose the smoothing parameter  $\lambda = 10^{-3}$  in (58). The linear equation obtained by the discretization of (59) is solved using Conjugate Gradient.

We also tested extreme anisotropies,  $\kappa \geq 100$  (thus  $\kappa_{\max} \geq 230$ ), which can be relevant in physics related applications. None of the tested schemes showed convincing results, and we thus refer to [4] for a radically different approach tailored for this setting.

The performance advantage of the AD-LBR is particularly clear when the error is measured in the  $H^1$  semi-norm: for the anisotropy  $\kappa = 10$  and the resolution  $500 \times 500$ , which are relevant values in image processing, AD-LBR outperforms its alternatives by a factor ranging from 3 to 5.

### 4.4 Coherence-enhancing diffusion

In order to document the interest of our discretization, we implement Coherence-Enhancing Diffusion [14] using the different numerical schemes at our disposal. The following parabolic equation is considered:

$$\partial_t u = \text{div}(\mathbf{D}(J_\rho(\nabla u_\sigma)) \nabla u). \quad (60)$$

This equation is non-linear since the diffusion tensor depends on the solution  $u$ , in addition to the four user defined parameters  $\sigma, \rho, C \in \mathbb{R}_+$ ,  $\alpha \in ]0, 1[$ . Let  $K_\sigma$  (resp.  $K_\rho$ ), be the Gaussian kernel of variance  $\sigma$  (resp.  $\rho$ ). Define the convolution  $u_\sigma := K_\sigma \star u$ , and the structure tensor  $J_\rho := K_\rho \star (\nabla u_\sigma \nabla u_\sigma^T)$ . The diffusion tensor  $\mathbf{D}(J_\rho)$  possesses the same eigenvectors  $(v_1, v_2)$  as  $J_\rho$ , and if the eigenvalues of  $J_\rho$  are  $\mu_1 \geq \mu_2$  then the eigenvalues of  $\mathbf{D}(J_\rho)$  are

$$\begin{aligned} \lambda_1 &= \alpha \\ \lambda_2 &= \alpha + (1 - \alpha) \exp\left(\frac{-C}{(\mu_1 - \mu_2)^2}\right). \end{aligned}$$

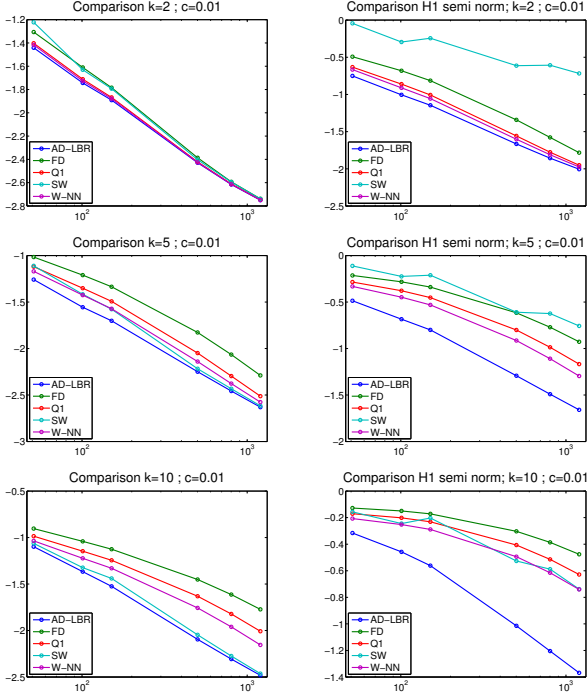


Figure 6: Left column: relative error in  $L^2$  norm (log-log scale) for different values of the anisotropy factor:  $\kappa = 2, 5, 10$ ; right column: relative error in  $H^1$  norm (log-log scale) for the same test cases.

This ensures that one smoothes preferably along the coherence direction  $v_2$ , with a diffusivity that increases with respect to the coherence  $(\mu_1 - \mu_2)^2$ . When the time parameter  $t$  becomes large, the image tends to a constant image, therefore it is necessary to stop the process at some finite time  $T$ . The ratio of the eigenvalues is bounded by  $\lambda_2/\lambda_1 \leq 1/\alpha$ , hence  $\kappa \leq 1/\sqrt{\alpha}$ .

We used an explicit time discretization for (60), with a time step  $\Delta t$ . The image  $u^{n+1}$  at time step  $(n+1)\Delta t$  is defined by the explicit equation:

$$\frac{u^{n+1} - u^n}{\Delta t} = \text{div}(\mathbf{D}(J_\rho(\nabla u^n))\nabla u^n).$$

The parameters used in our simulation were:  $\sigma = 0.5$ ,  $\rho = 4$ ,  $C = 10^{-5}$ ,  $\alpha = 10^{-2}$  and  $\Delta t = 0.02$ . This gives a maximum anisotropy of  $\kappa = 10$ . The algorithm was applied to a fingerprint image. The results obtained for  $T = 10$  are shown in Figures 7, 8 and 9 and they document the ability of our scheme to close interrupted lines more efficiently than the other schemes. The largest eigenvalue of the discrete operator  $-\text{div}(\mathbf{D}\nabla)$  at  $t = 0$  is given in Table 4 for the different schemes. As it was already noticed in the constant metric case, it turns out that AD-LBR has the smallest eigenvalues among all schemes, excepted scheme SW. This property allows (although this was not done in

Table 4: Largest eigenvalue of the discretized operator  $-\text{div}(\mathbf{D}\nabla)$ , where  $\mathbf{D} = \mathbf{D}(J_\rho(\nabla u_\sigma))$  at  $t = 0$ .

scheme	AD-LBR	FD	Q1	SW	W-NN
eigenvalue	3.75	5.67	5.09	0.96	3.83

our numerical experiments) to use larger time steps for AD-LBR than for the other schemes.

Note also that ridges are clearer, and valleys are darker, using AD-LBR than with the other schemes. (Gray-scale range is the same for all images, see also Figure 10). This reflects the fact that AD-LBR avoids, better than the other schemes, smoothing transversally to the orientation encoded in the continuous anisotropic PDE (60).

**Remark 3** (Computation time). *Numerical solvers of the parabolic PDE (60) combine three main components: (i) Constructing the diffusion tensor. (ii) Assembling the discretization stencils and the operator sparse matrix. (iii) Performing an explicit time step. Components (i) and (ii) are executed exactly the same number of times, while step (iii) is generally more frequent: in order to save CPU time, one typically does not update the operator at each time step. We produced a c++ implementation of AD-LBR, within the Insight Toolkit open source library. Although our code is neither parallel nor aggressively optimized, we believe that comparing the CPU times for steps (i), (ii) and (iii) is informative, and allows to estimate the additional cost of the AD-LBR which is essentially contained in step (ii).*

*For our 2D Coherence-Enhancing Diffusion (CED) experiment, on the  $512 \times 512$  fingerprint image, (i) takes 0.21s, (ii) 0.029s, (iii) 0.007s. For our 3D CED Experiment, on  $100 \times 100 \times 100$  synthetic data, (i) takes 1.35s, (ii) 0.55s, (iii) 0.052s. In both cases, the AD-LBR specific step (ii) is dominated by the construction of the diffusion tensor (i). Step (ii) is also dominated by the mere cost (iii) of iterations, provided the operator is updated less than once every 5 explicit steps in 2D (10 in 3D). To our eyes, the limited additional cost (ii) of AD-LBR is acceptable in view of the strong theoretical guarantees, and qualitative improvements, brought by this scheme.*

## 4.5 A 3-dimensional experiment

In order to illustrate the feasibility of our scheme in 3D space, we propose a synthetic example of plane-enhancing diffusion. The original image is a radially varying image in the cube  $[0, 1]^3$ , and the gray-level of the point  $x$  is defined to be

$$u^0(x) = \cos(2(r/R)^3),$$

where  $r = |x|$  and  $R = 1/2$  is a characteristic size of the oscillations. This image presents a series of concentric



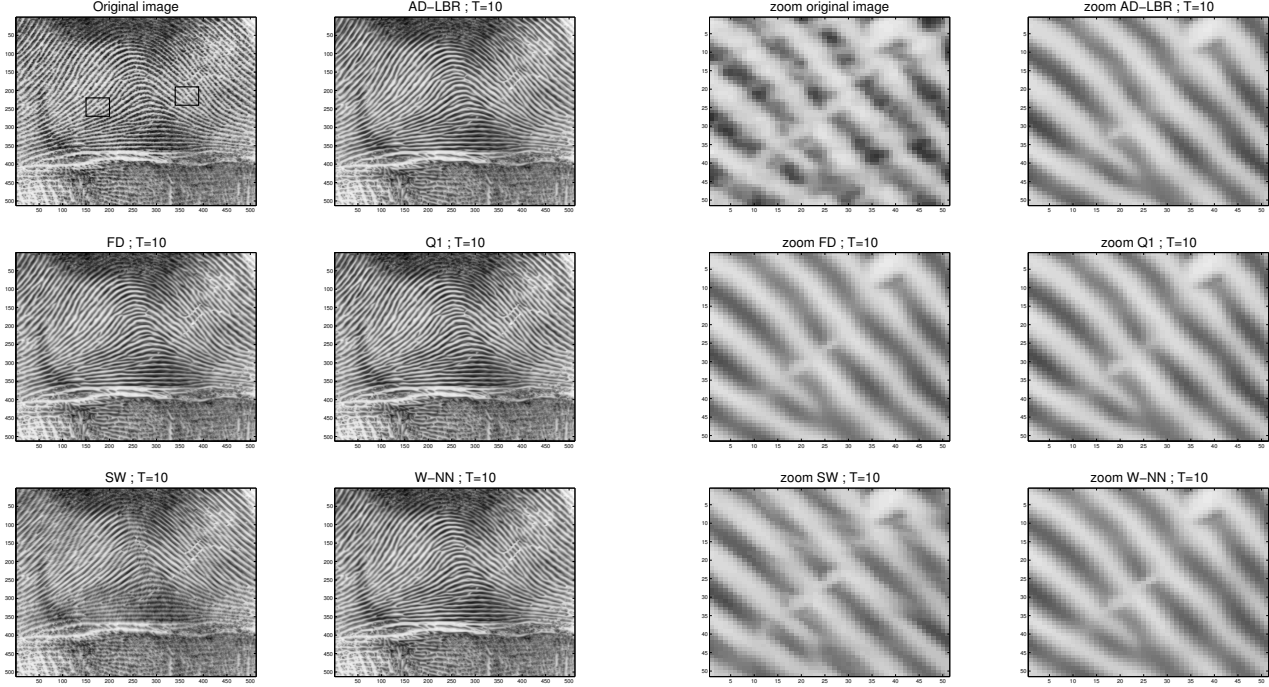


Figure 7: From top to bottom and from left to right: Original image (with two regions highlighted); diffused image using AD-LBR; FD; Q1; SW; W-NN. Here  $T = 10$ .

Figure 8: Detail of the region on the right. From top to bottom and from left to right: original image; diffused image using AD-LBR; FD; Q1; SW; W-NN.

level-sets. We present in Figure 11 the level sets  $\{u^0 = 0\}$ , and a slice through the plane  $z = 0.7$ .

The problem is discretized using  $100^3$  voxels. The image  $u^0$  is perturbed by

$$u = u^0 + n,$$

where  $n$  is an additive Gaussian noise of variance  $\sigma = 0.5$ . The reconstructed image is obtained using a 3D Coherence-Enhancing Diffusion PDE, similar to the 2D one in section 4.4:

$$\partial_t u = \operatorname{div}(\mathbf{D}(J_\rho(\nabla u_\sigma))\nabla u),$$

where  $J_\rho$  is the structure tensor defined by  $J_\rho = K_\rho \star (\nabla u_\sigma \nabla u_\sigma^T)$ ,  $u_\sigma = K_\sigma \star u$ . The tensor  $\mathbf{D}(J_\rho)$  possesses the same eigenvectors  $(v_1, v_2, v_3)$  as  $J_\rho$ , and if the eigenvalues of  $J_\rho$  are  $\mu_1 \geq \mu_2 \geq \mu_3$  then the eigenvalues of  $\mathbf{D}(J_\rho)$  are

$$\begin{aligned} \lambda_1 &= \alpha \\ \lambda_2 &= \alpha + (1 - \alpha) \exp\left(\frac{-C}{(\mu_1 - \mu_2)^2}\right), \\ \lambda_3 &= \alpha + (1 - \alpha) \exp\left(\frac{-C}{(\mu_1 - \mu_3)^2}\right), \end{aligned}$$

where  $\alpha = 10^{-2}$ . We used the values  $\sigma = 0.5$ ,  $\rho = 4$ . We present in Figure 11 the noisy image  $u$  (levelset 0 and planar slice) and the result after 20 time-steps of  $\Delta t = 10^{-3}$ .

## Conclusion

We introduced in this paper a new numerical scheme, AD-LBR, for anisotropic diffusion in image processing. This scheme is non-negative, and its stencils have a limited support: 6 points in 2D, 14 points in 3D. The former property implies that our scheme respects the maximum principle of Alvarez, Guichard, Lions and Morel, which is an essential feature of parabolic PDEs.

AD-LBR outperformed all alternatives known to us in a quantitative numerical experiment: a test case in which approximate numerical solutions are compared against a known analytical solution. In a second qualitative test case, different schemes were used to enhance a fingerprint image. Our scheme appears here to close more efficiently the lines of the fingerprint, and to diffuse less orthogonally to the lines. This is precisely the purpose of the implemented PDE, coherence enhancing diffusion. We also presented a 3-dimensional implementation as a proof of feasibility.

The construction of the stencils of the AD-LBR is both original and non-trivial. The computational load for this aspect of the algorithm is fortunately not dominant, thanks to the use of a tool from discrete geometry: lattice basis reduction. The AD-LBR also allows to use larger time steps than most of its counterparts, in explicit discretizations of parabolic equations.

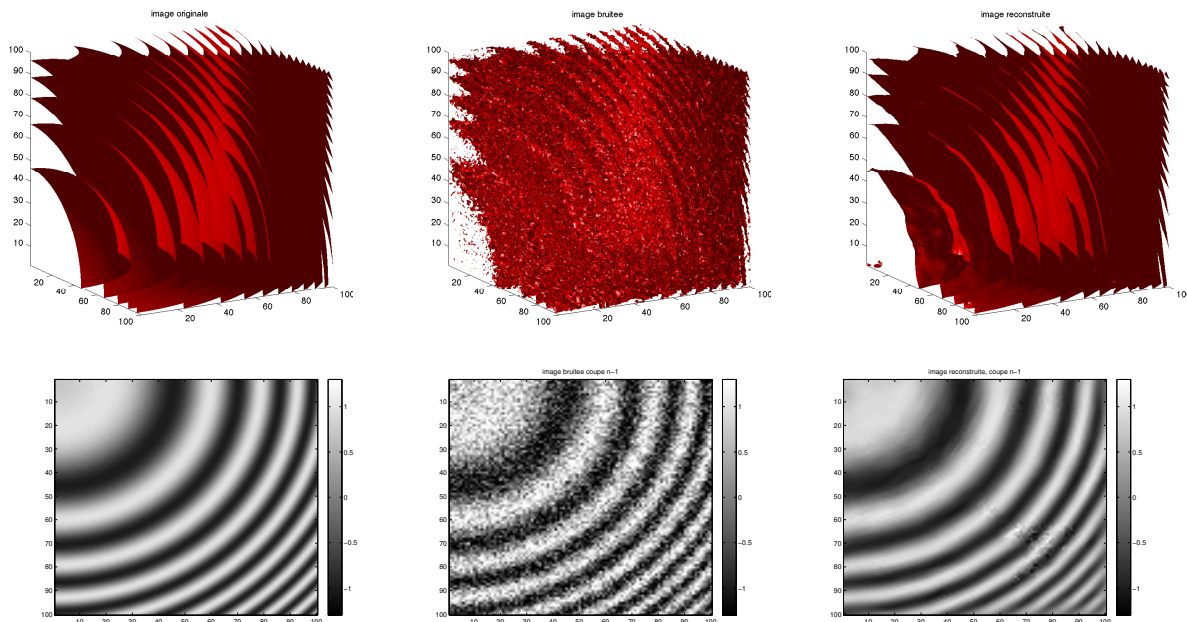


Figure 11: Levelset 0 (top) and slice (bottom) of a 3D image. Original (left), noisy (center), and reconstructed (right) images. Slice in the plane  $z = 0.7$ , with values clipped to the range  $[-1.3, 1.3]$ .

## References

- [1] L. Alvarez, F. Guichard, P.-L. Lions, J.-M. Morel, *Axioms and fundamental equations of Image processing*, Arch. Rational Mech. Anal., vol. 123, 199–257 (1993)
- [2] G.-H. Cottet, L. Germain, *Image processing through reaction combined with nonlinear diffusion*, Math. Comp., vol. 61, 659–673 (1993).
- [3] L. Dascal, A. Ditkowski, and N. Sochen, *On the Discrete Maximum Principle for the Beltrami Color Flow*, J. Math. Imaging Vision, vol. 29, 63–77 (2007)
- [4] P. Degond, A. Lozinski, J. Narski, C. Negulescu, *An Asymptotic-Preserving method for highly anisotropic elliptic equations based on a micro-macro decomposition*, J. Comput. Phys., vol. 231(7), 2724–2740 (2012)
- [5] F. Labelle, J. R. Shewchuk, *Anisotropic Voronoi Diagrams and Guaranteed-Quality Anisotropic Mesh Generation*, Proceedings of the Nineteenth Annual Symposium on Computational Geometry, 191–200 (2003)
- [6] J.-M. Mirebeau, *Anisotropic Fast Marching on Cartesian Grids, using Lattice Basis Reduction*, preprint, 2012.
- [7] J.-M. Mirebeau, *On the Accuracy of Anisotropic Fast Marching*, preprint.
- [8] J.-M. Mirebeau, *Efficient Fast Marching with Finsler Metrics*, preprint.
- [9] P. Q. Nguyen, and D. Stehlé, *Low-dimensional lattice basis reduction revisited*, ACM Transactions on Algorithms, Article 46 (2009).
- [10] S. Osher, L. Rudin *Feature-oriented image enhancement using shock filters*, SIAM J. Numer. Anal., vol. 27, 919–940 (1990)
- [11] P. Perona and J. Malik, *Scale-Space and Edge Detection Using Anisotropic Diffusion*, IEEE Trans. Patt. Anal. Mach. Int., vol. 12, 629–639 (1990)
- [12] C. Schmaltz, J. Weickert, and A. Bruhn, *Beating the Quality of JPEG 2000 with Anisotropic Diffusion* (2009)
- [13] J. Weickert, *Theoretical foundations of anisotropic diffusion in image processing*, Computing, SUPPL. 11, 221–236 (1996)
- [14] J. Weickert, *Anisotropic Diffusion in Image Processing*, Teubner, Stuttgart (1998)
- [15] J. Weickert, B. Romeny, and M. Viergever, *Efficient and reliable schemes for nonlinear diffusion filtering*, IEEE Trans. Image Proc., vol. 7, 398–410 (1998)
- [16] J. Weickert, and H. Scharr, *A scheme for coherence-enhancing diffusion filtering with optimized rotation invariance*, J. Visual Comm. Image Rep., Vol. 13, 103–118, (2002).

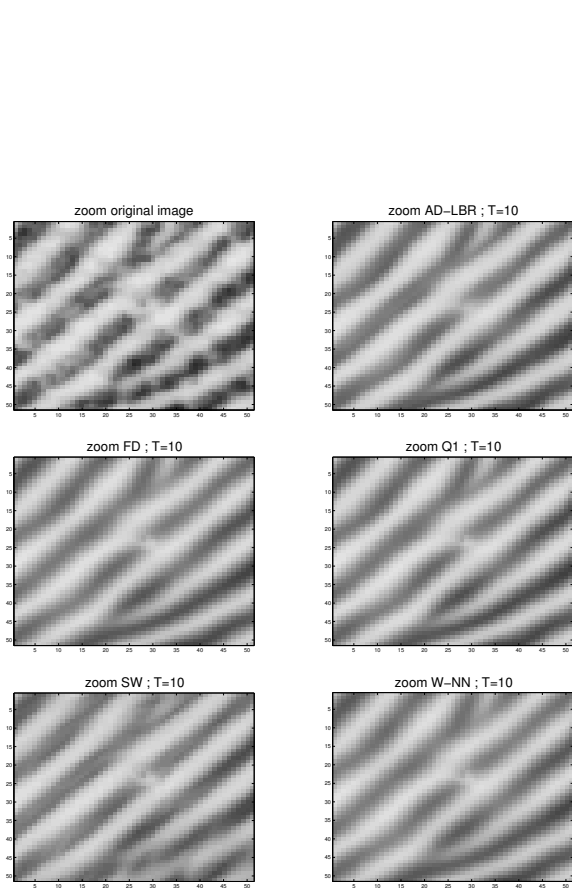


Figure 9: Detail of the region on the left. From top to bottom and from left to right: original image; diffused image using AD-LBR; FD; Q1; SW; W-NN

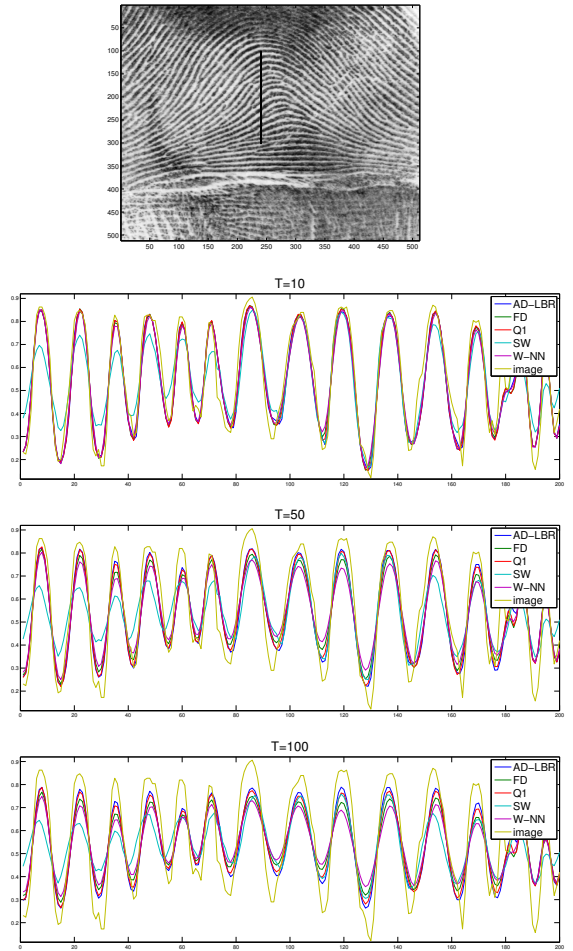


Figure 10: Evolution under CED of a section of the fingerprint image. The ridges in the evolved image are higher, and the valleys are deeper, with AD-LBR than with the other schemes. This illustrates the fact that AD-LBR, respecting the continuous PDE, diffuses more along the structure and less in the orthogonal direction. From top to bottom: location of the section of the image; section at  $T = 10$ ; section at  $T = 50$ ; section at  $T = 100$ .